Title

Deep Circulation, Contaminant Mobility, and Seafloor Observations in San Pedro Basin, CA

ISBN

9798190941395

Author

Kreitzer, Zachary Austin

Publication Date

2026-09-15

Peer reviewed|Thesis/dissertation

UNIVERSITY OF CALIFORNIA SAN DIEGO

Deep Circulation, Contaminant Mobility, and Seafloor Observations in San Pedro Basin, CA

A thesis submitted in partial satisfaction of the
requirements for the degree Master of Science

in

Oceanography

by

Zachary Austin Kreitzer

Committee in charge:

Sophia Merrifield, Chair
Eric Terrill, Co-Chair
Ryan McCarthy
Gunnar Voet

2026

The Thesis of Zachary Austin Kreitzer is approved, and it is acceptable in quality and form for publication on microfilm and electronically.

University of California San Diego

2026

DEDICATION

To those with whom I’ve sailed the seas,

To all who’ve treated me with love, patience and care,

To those who’ve shaped my heart , soul and mind,

I am eternally grateful.

EPIGRAPH

For instance, on planet Earth, man had always assumed that he was more intelligent than dolphins because he had achieved so much - the wheel, New York, wars and so on - whilst all the dolphins had ever done was muck about in the water having a good time. But conversely, the dolphins had always believed that they were far more intelligent than man, - for precisely the same reasons.

Douglas Adams, *The Hitchhiker's Guide to the Galaxy*

Don't sabotage yourself. There are plenty of other people willing to do that for free.

Jenny Lawson, *Furiously Happy*

Optimism is true moral courage.

Sir Ernest Shackleton

TABLE OF CONTENTS

Thesis Approval Page iii

Dedication iv

Epigraph v

Table of Contents vi

List of Figures viii

Acknowledgements xi

Vita xiii

Abstract of the Thesis xiv

Chapter 1 Introduction 1

Chapter 2 Observations 5
2.1 SPOT Hydrographic Record 5
2.2 Niño 3 Index 7
2.3 Mooring Deployments 7
2.4 Sediment Cores 10
2.5 AUV Acoustic Imagery 11
2.6 ROV Imagery 11

Chapter 3 Deep Water Circulation 12
3.1 Flushing Events 12
3.2 Seasonal variability 14
3.3 ENSO variability 15
3.4 Subtidal, Inertial and Tidal Variability 16

Chapter 4 Sediment Resuspension Events 23
4.1 Bottom Boundary Layer Structure 23
4.2 Resuspension Events 27

Chapter 5 Seafloor Imagery 34
5.1 Sediment Cores 34
5.2 Acoustic and Optical Imagery 38
5.3 Biogenic Processes 40

Chapter 6 Conclusions and Future Work 41
6.1 Conclusions 41
6.2 Future Work 44

Bibliography 47

LIST OF FIGURES

Figure 2.1. Bathymetric map of the San Pedro Basin and surrounding region [6]. The map shows the SPOT survey site (blue circle) and the 2024 mooring deployment location (red triangle). 6

Figure 2.2. Profiles of SPOT variables across 20 years of data in the SPB. Thick black lines represent the mean of all casts, while grey lines represent the individual casts. 7

Figure 2.3. CTD observations for depths below the sill (740 meters). 8

Figure 2.4. Schematic of the SPB mooring configuration used in both 2023 and 2024 deployments. The dissolved oxygen sensor mounted near the bottom experienced mechanical issues, which prevented the collection of oxygen data [24]. 9

Figure 2.5. Time series of near-bottom horizontal velocity measured by the ADCPs during the (a) 2023 and (c) 2024 mooring deployments. (b) and (d) represent depth-averaged time series. 10

Figure 3.1. Time series of deep-basin temperature and oxygen exchange across major sill regions in the SCB, from [19]. The relatively weak variability in SPB compared to neighboring basins highlights the restricted nature of exchange below the sills. 13

Figure 3.2. Temperature–salinity (T–S) diagrams for the San Pedro Basin water column. (a) Full-depth profiles illustrate the overall water mass structure, while (b) a zoom of the bottom 50 m highlights the weak thermal and salinity gradients characteristic of the isolated deep layer. 14

Figure 3.3. Monthly climatology of potential density (σ_0) from SPOT observations. Error bars represent the standard deviation across all years. Overlaid markers indicate corresponding measurements from the 2024 mooring deployment (SBE37), showing general agreement with the long-term seasonal cycle. . . 15

Figure 3.4. Relationship between dissolved oxygen concentrations from SPOT and the Niño 3 index in the deep San Pedro Basin (850–900 m). Data are grouped by season to assess potential seasonal variability. The large scatter and weak trend indicate minimal influence of ENSO on deep oxygen variability. 16

Figure 3.5. Power spectral density of depth-averaged U and V currents from the 2024 ADCP mooring deployment. Peaks at diurnal and semidiurnal frequencies indicate dominant tidal forcing, with additional energy near the inertial frequency. 18

Figure 3.6. Two-dimensional histogram (heatmap) of horizontal current velocities (U and V) from the 2024 mooring deployment. Color shading represents the frequency of occurrence, with warmer colors indicating more frequent velocities. 19

Figure 3.7. Tidal current ellipses for the dominant constituents derived from the 2024 ADCP data. Ellipse orientation and magnitude illustrate the directional structure and strength of tidal currents in the deep San Pedro Basin. 20

Figure 3.8. Rotary spectra of depth-averaged ADCP currents. Clockwise and counter-clockwise components highlight energy partitioning, with peaks at tidal and near-inertial frequencies indicating dominant forcing mechanisms. . . . 21

Figure 4.1. Vertical structure of the leading EOF modes for the horizontal currents. The left panel shows the U (east–west) component, and the right panel shows the V (north–south) component. The dominant mode captures the primary depth-dependent structure of the flow in the lower water column. . 24

Figure 4.2. Percent variance explained by empirical orthogonal function (EOF) modes for U and V currents from the 2024 mooring deployment. The first mode captures the majority of variance, indicating a dominant flow structure. . . . 25

Figure 4.3. Time–depth evolution of horizontal currents (U and V) from the 2024 mooring deployment. Color shading represents velocity magnitude, highlighting temporal variability and depth structure in the flow field. 26

Figure 4.4. Time–depth evolution of current anomalies (U and V) from the 2024 mooring deployment after removal of the mean. Anomalies emphasize variability associated with tidal and subtidal processes. 26

Figure 4.5. Time series of horizontal velocities and total current speed measured at 2 m HAB during the 2024 mooring deployment. The upper two panels show the east-west (U), and north-south (V) velocity components, while the bottom panel shows the horizontal current speed. 30

Figure 4.6. Time series of bed shear stress estimated using the drag-law formulation at 2 m HAB from the 2024 ADCP mooring deployment. Horizontal lines represent critical Shields-based erosion thresholds calculated for representative representative grain sizes of 4 μm, 8 μm, and 63 μm. 31

Figure 4.7. Upper panel: Time series of estimated bed shear stress (τ_b) calculated using the quadratic drag-law approach from observed horizontal current speeds at 2 m HAB. Dashed horizontal lines indicate empirical critical shear stress thresholds for cohesive sediment erosion 32

Figure 4.8. Critical velocity required to exceed modeled cohesive sediment erosion thresholds as a function of drag coefficient C_D for two representative dry-bulk densities observed in SPB sediments ($\rho_d = 165$ and $\rho_d = 330\ \frac{kg}{m^3}$). . . . 33

Figure 5.1. Bathymetric map of the San Pedro Basin showing the locations of 54 sediment cores. Color shading and contour lines represent seafloor depth, while dashed circles indicate the primary ocean disposal sites (DS1 and DS2). . . . 35

Figure 5.2. Interpolated spatial distributions of sediment core-derived properties across the San Pedro Basin: (A) Depth of maximum DDT concentration (cm), (B) maximum ΣDDT concentration at depth, and (C) maximum ΣDDX concentration. . . . 36

Figure 5.3. Locations of three representative sediment cores selected for detailed analysis. These cores span regions of varying DDT accumulation and sedimentary environments, allowing for comparison of contaminant penetration and vertical structure across the basin. . . . 37

Figure 5.4. Vertical profiles of ΣDDT and ΣDDX concentrations for three selected sediment cores plotted as a function of sediment depth. All cores exhibit subsurface concentration maxima at approximately 5–10 cm. . . . 38

Figure 5.5. Representative SAS imagery(A-C) of the San Pedro Basin seafloor. The vehicle operated at a constant altitude of approximately 30 m above the seafloor, producing swath ranges of 72 m (A17), 158 m (C20), and 88 m (T2-d). . . . 39

Figure 6.1. The colored surface shows the spatial distribution of maximum ΣDDT concentrations from sediment cores. . . . 45

ACKNOWLEDGEMENTS

I would like to acknowledge all of the wonderful scientists, engineers, and all the lovely humans in between who have made my time at CORDC so wonderful. Thank you all—you are truly incredible people whom I have been blessed to learn from.

I'd like to thank Dr. Eric Terrill for his steadfast leadership, help and knowledge, Dr Gunnar Voet for his kindness and wonderful insights.

Thank you, Dr. Sophia Merrifield, for all the guidance, care, and many hours of mentorship throughout this process. The bravery you've shown during your own struggles, and the way you've shown up for your students and everyone in the lab, is an exemplary demonstration of true leadership.

I must thank Dr. McCarthy, as without him I would not have made it. You have been a wonderful fountain of knowledge, patience, and genuine care. You never let me forget that I was capable and that I just needed to keep going. Good luck in Hawaii, and see you next time, man! A special thanks and best wishes to Ted, Adam, John, Kat, and all the graduate students and postdoctoral researchers I've met along this journey. Thank you to Justin, Anuj, Kyle, Professors Mark Merrifield and Janet Becker (and Janet's cat, a true MVP). You have all helped me get to where I am today.

A special thanks to Sean Celona for helping me navigate all the data and woes associated with long-term data records. You're a real MVP!

Thank you to Sean McPeak, Jorge, Cole, Jit, Derrick, and the rest of the crew. Thank you for the friendship, fun conversations, and all the engineering knowledge you have imparted.

A very special thank you to my family is also in order.

Thank you to my father, Bob, for instilling in me a love of science, literature, libraries, and the pursuit of knowledge.

To my mother, Barb, thank you for the constant love, care, and compassion she has shown me throughout my life, and for instilling in me a sense of levity, empathy, and a deep love for the natural world.

To my sisters, Zoe and Hannah, thank you for your support and for helping me learn not to take life *too* seriously, while also appreciating the art and beauty the world has to offer.

To my brothers-in-law, Brett and Max, thank you for being great men and for treating my sisters with the care and compassion they deserve. You are the best brothers I could have asked for.

To Bear, Oona, Malakai, and Wyatte: I love you all, you feral goobers. I can't wait to watch you grow into your own.

VITA

2025–2026 Master of Science, University of California San Diego

2022–2025 Bachelor of Science, University of California San Diego

2020–2022 Liberal Arts and Sciences, Science Studies, Physics, Mesa Community College, San Diego

2014–2019 U.S. Navy

2009–2013 Bangor High School

FIELDS OF STUDY

Major Field: Oceanic and Atmospheric Science

ABSTRACT OF THE THESIS

Deep Circulation, Contaminant Mobility, and Seafloor Observations in San Pedro Basin, CA

by

Zachary Austin Kreitzer

Master of Science in Oceanography

University of California San Diego, 2026

Sophia Merrifield, Chair
Eric Terrill, Co-Chair

The San Pedro Basin (SPB) is a deep borderland basin in the Southern California Bight containing DDT-contaminated sediments, yet the physical processes governing sediment mobilization, transport, and redistribution remain poorly constrained. This study integrates long-term hydrographic observations from the San Pedro Ocean Time-series (SPOT) with near-bottom mooring measurements to characterize deep-ocean circulation, bottom boundary-layer dynamics, and sediment resuspension potential. Hydrographic observations indicate weak stratification below the 740 m sill and minimal seasonal or interannual variability, consistent with prolonged isolation of deep-basin waters. Relationships between deep-water density, dissolved oxygen, and the Niño 3 index are weak, suggesting limited penetration of ENSO-related variability into the deep basin. Near-bottom Acoustic Doppler Current Profiler (ADCP) measurements show that bottom current variability is dominated by semidiurnal tides, with secondary contributions from diurnal and near-inertial motions. Estimated bed shear stresses were generally weak, with intermittent spring tide maxima approaching theoretical erosion thresholds. Comparisons with cohesive sediment erosion models suggest that widespread resuspension is unlikely under typical conditions. Seafloor imagery collected at the sediment core locations shows evidence of biogenic activity, suggesting a potential pathway for sediment suspension and subsequent water column transport, in addition to the potential for contaminant transfer into the marine food web. Together, these results suggest that deep SPB circulation is dominated by weak tidal forcing that intermittently enhances bottom shear stress while promoting long-term retention of contaminated sediments within the basin.

Chapter 1

Introduction

Throughout the twentieth century, deep-water disposal of military, industrial, and chemical waste was common along the U.S. coastlines, based on the assumption that dilution and dispersion in the open ocean would minimize long-term environmental impacts [30, 15]. In the Southern California Bight (SCB), this practice was particularly extensive, with one of the most consequential and long-lasting examples being the large-scale production and offshore disposal of dichlorodiphenyltrichloroethane (DDT) [18, 21]. Regulated discharges were permitted through the Los Angeles sewer outfall system, which terminates at the nearby Palos Verdes Shelf [15]. However, subsequent investigations demonstrated that these permitted discharges alone cannot account for the observed extent of deep-sea contamination [15, 30]. The Montrose Chemical Company was the primary source of coastal DDT waste, producing approximately 800,000 tons of the hydrophobic pesticide between 1947 and 1982 [11].

Optical surveys have confirmed debris and barrel-like objects throughout the San Pedro Basin (SPB), reinforcing the scale and long-term anthropogenic contamination in the seabed ([15], [24]). The SPB is the southernmost basin within the SCB and lies between the Los Angeles coastline and Santa Catalina Island. It is approximately 40 km wide, 100 km long, and deepens to nearly 900 m. The two primary regions identified in previous studies are located near the northeastern slope of Santa Catalina Island (dumpsite 1; DS1) and across the central plain of SPB (dumpsite 2; DS2) (Figure 2.1). Disposal of DDT waste in the basin is estimated to include more than 300,000 objects that potentially contained more than 1,500 tons of pesticide and industrial waste from its production [11, 20]. High-resolution side-scan sonar surveys have identified more than 27,000 barrel-like targets distributed across at least two major dumpsites within the basin, identified as spatially distinct debris fields in recent surveys [20]. The spatial distribution of the debris fields suggests that the multiple pathways of disposal contributed to the heterogeneous distribution of DDX throughout the basin. These debris fields modify near-seafloor habitats and may act as localized sources of chemical leakage, further enhancing contamination within the basin.

The ecological consequences of exposure to DDX have been widely documented in both marine and terrestrial systems. Elevated contaminant burdens and corresponding increases in cancer prevalence have been documented in multiple upper trophic-level species [17, 18, 21]. Disruptions of endocrine function, eggshell thinning, reproductive abnormalities, cancers, and developmental problems have been observed in birds, fish, marine mammals, and humans as a result of exposure [9, 18, 2]. Remotely Operated Vehicle (ROV) has documented the benthic communities inhabiting sediments surrounding the dumpsites, including polychaetes, meiofauna, suspension feeders, and other macrofauna organisms [21, 22]. Through burrowing, sediment reworking, and feeding activity, these organisms may disturb local shallow contaminant zones, facilitating uptake into their bodies and creating pathways of trophic transfer into the local ecosystem. The persistence of these compounds, coupled with limited degradation rates in deep, low-oxygen environments, underscores ongoing exposure risks to marine ecosystems and coastal human populations. Although chemical fate and biological accumulation pathways have been extensively studied, comparatively less is known about the physical mechanisms responsible for mobilizing contaminated sediments and redistributing DDX within the basin and across the broader SCB. While contamination is distributed across 2 main disposal sites in SPB, this study focuses on DS2, where the recent mooring observations and coring studies have been concentrated.

Recent sediment analyses from DS2 revealed localized DDT and its degradation products

(DDX) concentrations up to approximately forty times greater than the highest surface sediment concentrations measured at the nearby Palos Verdes Shelf Superfund site, indicating extensive direct offshore dumping [15]. These findings indicate that the basin represents a highly contaminated deep-sea environment, with sediment DDX concentrations far exceeding those observed at other sites in the region [15, 30]. Sediment cores collected in SPB show peak levels of DDX are most consistently 4-8 centimeters below the seafloor [22]. This subsurface maximum suggests burial following peak deposition in the mid-20th century.

The geometry of the SPB features steep sidewalls bounded by a narrow inter-basin sill—an elevated seafloor feature at roughly 740 m depth—that restricts basin-to-basin water exchange [13, 10]. Below this sill depth, basin waters become dynamically isolated from surrounding source waters, leading to prolonged residence times and weak vertical ventilation. The renewal of SPB bottom waters occurs episodically when dense, oxygen-rich water masses overflow the sill from the neighboring Santa Monica Basin [19]. Known as flushing events, these intrusions are identified by abrupt decreases in temperature accompanied by localized increases in dissolved oxygen concentrations. These episodic renewal events induce density and velocity perturbations that may play a role in intermittently enhancing near-bottom shear stress. Such renewal events are irregular in timing and magnitude, occurring over subannual to multi-year intervals [13, 19]. Modeling and observational studies estimate deep-water renewal timescales of one year or longer, comparable to ventilation times in other semi-enclosed borderland basins [19]. As a result, deep SPB waters remain weakly stratified and suboxic for extended periods.

The physical isolation of SPB and the episodic nature of deep-water renewal suggest that sediment resuspension and lateral particle transport are controlled by intermittent forcing. Basin-scale circulation reflects a combination of eddy-driven along-slope flows and intermittent cross-sill pressure gradients associated with deep-water renewal [19, 12]. Superimposed on these motions are tidal currents that dominate near-bed velocity variance throughout the basin [12]. Independent sediment trap observations indicate that episodic resuspension events and lateral transport into the basin contribute substantially to vertical and lateral particle fluxes in SPB [5, 25].

Bottom boundary layer processes, including oscillatory tidal flows and periodic enhancement of near-bed shear stress, have been shown elsewhere to mobilize fine-grained sediments under similar physical regimes [16, 26]. Whether tidal forcing alone or in combination with flushing events is sufficient to exceed the critical thresholds for DDX-bearing mud resuspension in SPB remains unresolved.

Large-scale climate variability may further influence the dynamics of the deep basin. ENSO influences regional stratification, source water properties, and circulation throughout Southern California [14, 3]. Understanding whether these large-scale signals propagate to the bottom boundary later is important for evaluating the potential role in sediment resuspension and contaminant transport. However, it remains unclear to what extent interannual climate forcing penetrates to the sill depth and affects deep basin renewal or sediment mobility. Together, these uncertainties limit current understanding of the physical pathways that govern the redistribution of DDX-contaminated sediments throughout the SPB and across the SCB. This study uses deep-basin observations to characterize near-bottom flow variability, assess bottom shear stress, and evaluate the potential for sediment resuspension in SPB.

Chapter 2

Observations

This study uses datasets to investigate circulation and sediment resuspension processes in the SPB: (1) long-term hydrographic profiles from the San Pedro Ocean Time-series (SPOT) [27] , (2) high-frequency near-bottom current measurements from moored instruments, (3) the Niño 3 index, used to place local variability within the broader climatic context of ENSO forcing, (4) sediment cores, (5) AUV acoustic imagery, and (6) ROV optical imagery. Together, these records provide a view of basin variability across seasonal, interannual, and tidal timescales, allowing large-scale forcing to be evaluated alongside local boundary-layer dynamics, and enabling assessment of how variability across these scales influences near-bottom circulation and potential sediment resuspension within the basin.

2.1 SPOT Hydrographic Record

The SPOT program conducts monthly oceanographic cruises in the SPB that collect hydrographic and biogeochemical data using Conductivity–Temperature–Depth (CTD) profiling. Sampling locations were primarily around dumpsite 2 as seen in Figure 2.1. These samples include temperature, salinity, conductivity, pressure, and dissolved oxygen. Each cruise includes one to five CTD casts depending on sampling needs. The SPOT archive spans 2000–2024 (with limited sampling during the early COVID-19 pandemic) and represents the longest continuous record of physical and chemical properties within the basin. This dataset provides the primary

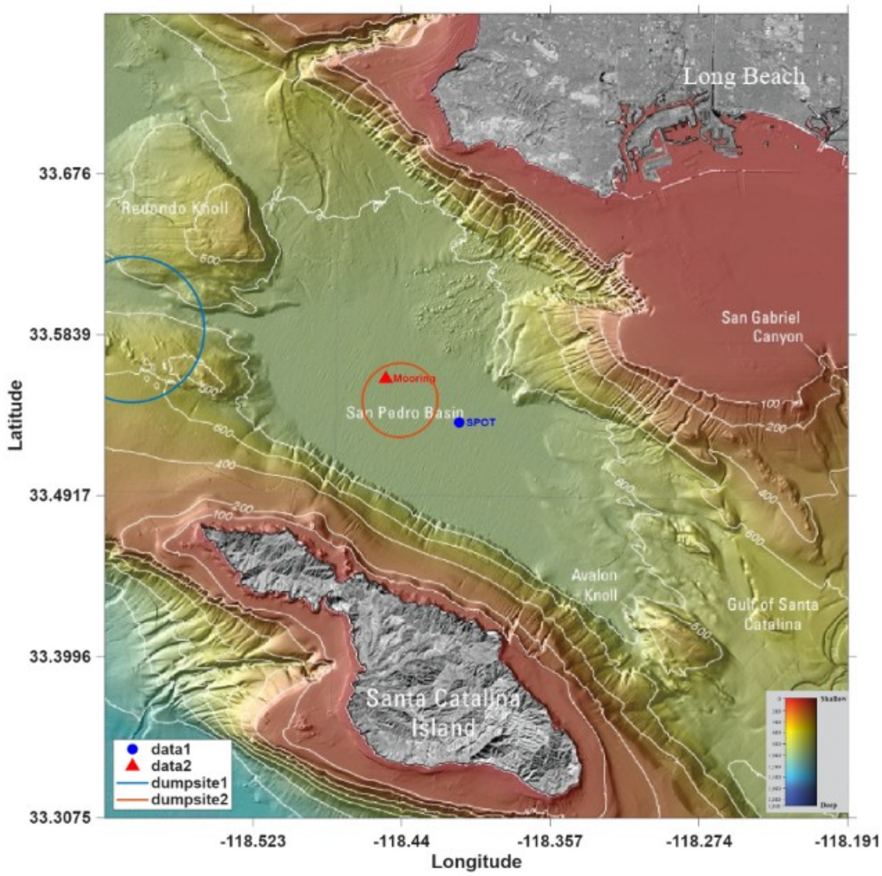

Figure 2.1. Bathymetric map of the San Pedro Basin and surrounding region [6]. The map shows the SPOT survey site (blue circle) and the 2024 mooring deployment location (red triangle).

observational context for assessing background hydrographic stability and identifying potential deep-water renewal signals across seasonal and interannual timescales. In particular, variations in temperature and potential density at depths below the sill provide key indicators of episodic bottom water renewal and the introduction of new water masses into the basin.

CTD cast measurements are shown in Figures 2.2 and 2.3. Potential density and oxygen saturation are derived during post-processing. Data are reported at 1-m vertical resolution and extend to approximately 900 m, encompassing the full depth of the basin. Routine quality-control procedures remove negative or spurious oxygen values resulting from sensor drift. Despite intermittent gaps, the SPOT program provides a robust baseline for evaluating low-frequency variability in bottom-water properties, allowing transient renewal events to be distinguished from

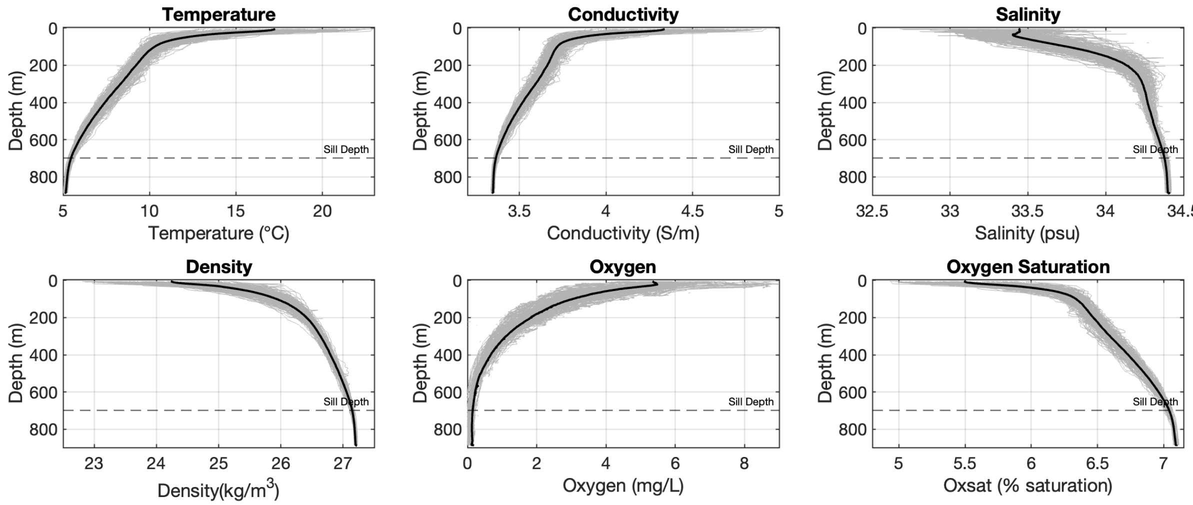

Figure 2.2. Profiles of SPOT variables across 20 years of data in the SPB. Thick black lines represent the mean of all casts, while grey lines represent the individual casts.

seasonal and interannual background variability.

2.2 Niño 3 Index

The Niño 3 index (5° S–5° N, 150° W–90° W) was obtained from NOAA's Climate Prediction Center as a standardized metric of the ENSO phase. Monthly values were interpolated onto SPOT cruise dates and analyzed for correspondence with density anomalies observed in deep SPB waters. This index provides a basin-scale climate forcing reference against which local hydrographic variability and renewal processes can be evaluated. ENSO-driven variability influences the regional stratification of source water properties. This may modulate the density structure of water masses entering the basin and thereby affect the frequency and intensity of deep water renewal events.

2.3 Mooring Deployments

To complement the long-term SPOT record, near-bottom moorings (Figure 2.1) were deployed to capture high-frequency velocity and hydrographic variability within the bottom boundary layer, which governs near-bed shear stress and controls the potential for sediment

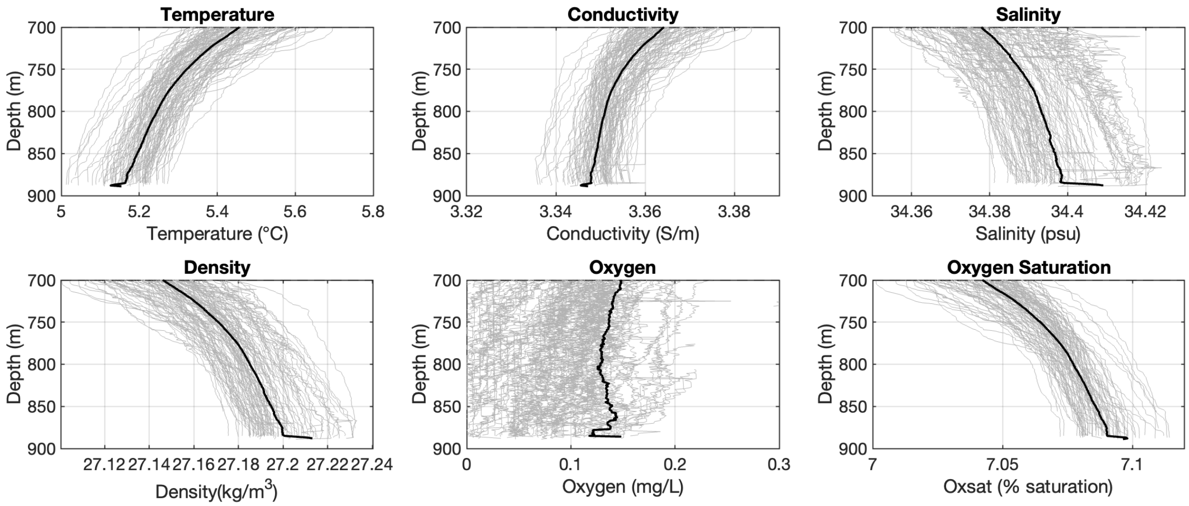

Figure 2.3. CTD observations for depths below the sill (740 meters).

resuspension. These measurements resolve tidal and subtidal flow variability that cannot be captured by monthly shipboard sampling. Each mooring (Figure 2.4) was equipped with a downward-facing 600 kHz Teledyne Marine ADCP positioned approximately 38 m above the seafloor and a Sea-Bird SBE37 MicroCAT mounted 1.5 m above bottom, measuring temperature, conductivity, and dissolved oxygen [24].

The ADCP recorded three-dimensional current velocities from 0 to 38 m above bottom with 2-m vertical bins. Sampling employed 2-minute ensembles (6-minute for the 2023 deployment), resolving semidiurnal and diurnal tidal motions as well as higher-frequency internal wave variability (Figure 2.5a,c). Maximum observed depth averaged velocities were 15 cm/s (Figure 2.5b,d). These measurements provide the temporal resolution needed to quantify the variability in the near-bottom flow velocities and assess the magnitude and intermittency of shear stress forcing along the seafloor. The SBE37 collected 1-Hz burst samples lasting 12 minutes at 9-second intervals, providing high-resolution temperature and salinity measurements adjacent to the seabed, which helps constrain density variability associated with renewal events.

The 2023 mooring (March 3 – July 7) suffered line stretching that elevated the ADCP beyond its intended depth; these data are excluded from subsequent analyses. The 2024 deployment (late January – early July) produced the complete high-quality dataset used for boundary

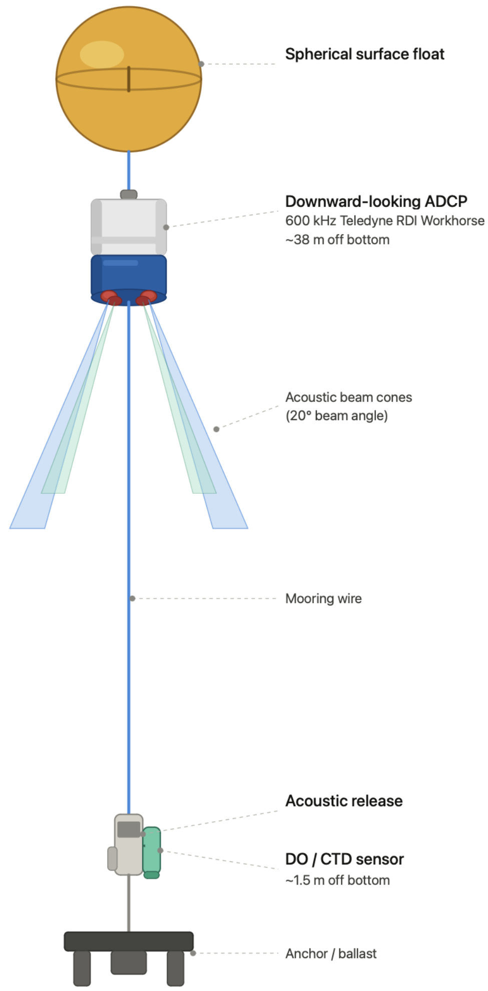

Figure 2.4. Schematic of the SPB mooring configuration used in both 2023 and 2024 deployments. The dissolved oxygen sensor mounted near the bottom experienced mechanical issues, which prevented the collection of oxygen data [24].

layer velocity and hydrographic analyses in this study. The dissolved oxygen sensors on both moorings exhibited drift and eventual failure, but the temperature and salinity records remained reliable throughout both deployments. The 2024 deployment record provides the primary dataset for evaluating the near-bottom flow variability and its role in the remobilization of sediment.

The combined datasets are limited by the sparsity of sampling and the lack of continuous dissolved-oxygen measurements within the bottom boundary layer of SPB. SPOT surveys provide monthly hydrographic profiles at a single central-basin location, while dissolved oxygen sensors on the moorings experienced drift and failed prior to the conclusion of their deployments. Conse-

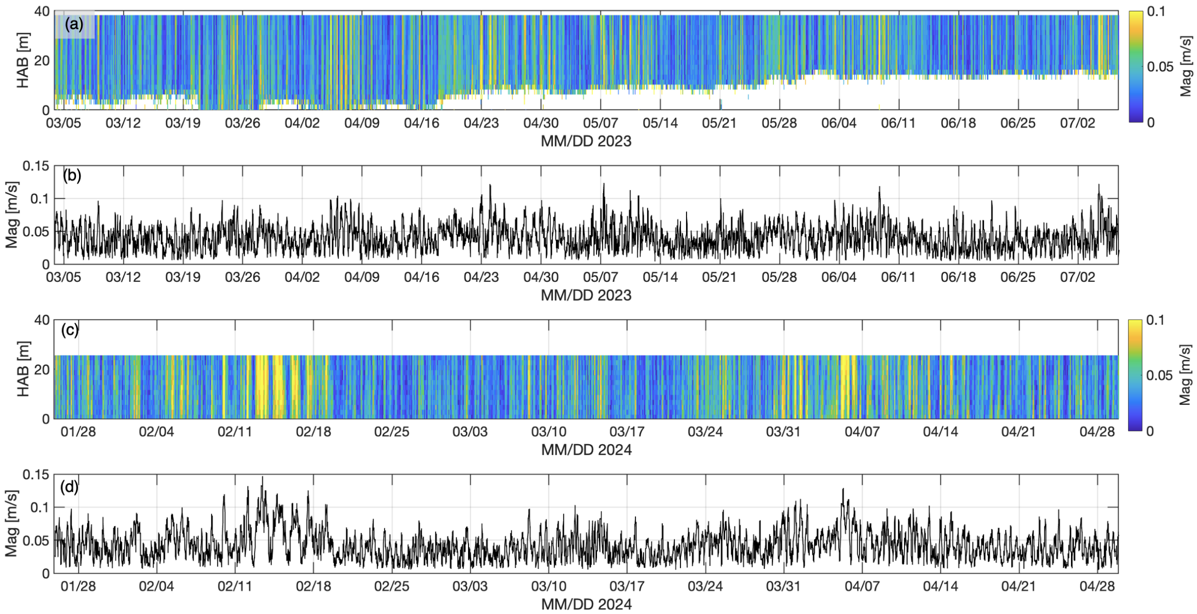

Figure 2.5. Time series of near-bottom horizontal velocity measured by the ADCPs during the (a) 2023 and (c) 2024 mooring deployments. (b) and (d) represent depth-averaged time series.

quently, assessments of deep-water renewal rely primarily on hydrographic proxies—particularly temperature and potential density—rather than direct measurements of near-bed oxygen variability, which introduces uncertainty in identifying the timing and intensity of possible renewal events.

2.4 Sediment Cores

Sediment core datasets from [30] and [22] were used to characterize the spatial distribution of contaminants, burial structure, and sediment properties across SPB. Core samples were collected during multiple cruises using sediment multicorers and targeted sampling near the primary disposal regions. A total of 54 sediment cores distributed across the basin were used to examine the vertical distribution and preservation of DDT and related degradation products within SPB sediments. The datasets include vertically resolved measurements of ΣDDT and ΣDDX, along with individual concentrations of DDD and DDE compounds used to evaluate contaminant distributions throughout the basin.

2.5 AUV Acoustic Imagery

Autonomous underwater vehicle (AUV) surveys were conducted using the HUGIN platform equipped with a High-resolution Interferometric Synthetic Aperture Sonar (HISAS) system. HUGIN operated at 30m altitude and included swath widths of $\sim$ 180m in the across-track on both the port and starboard. Data were postprocessed to a resolution of $\sim$ 2cm. Surveys were designed to characterize seafloor morphology, sediment texture, and spatial patterns in acoustic backscatter across the study region. The HUGIN vehicle operated along pre-programmed survey lines at low altitude above the seabed to maximize sonar resolution and spatial coverage. The HISAS system produced georeferenced acoustic imagery with 4cm square pixel resolution, enabling the identification of fine-scale seabed features.

2.6 ROV Imagery

Additional seafloor observations were collected using the CURV-21 ROV system equipped with forward-looking video and still-imaging capabilities. The ROV operated within the same footprint as the AUV at $\sim$ 1m height above the seafloor and captured $\geq$ 300 hours of video imagery. Data was collected in both DS1 and DS2 following areas of interest from the HISAS imagery. These observations provided direct visual ground truth for the interpretation of the acoustic backscatter signatures observed in the HISAS mosaics. Video transects were used to identify sediment type, benthic habitat characteristics, anthropogenic debris, and biological communities that could not be uniquely resolved from acoustic data alone.

Chapter 3

Deep Water Circulation

SPB's deep water remains isolated below the sill for extended periods (700–900 m), and renewal of bottom water is infrequent and poorly constrained. While circulation above the sill is characterized by a cyclonic mean flow along the basin perimeter [12], the dynamics of the near-bottom layer remain less well understood. This study focuses on the 50 m of the water column adjacent to the seabed, where processes governing sediment transport are most critical.

To investigate the near-bottom environment, we combine multi-decadal SPOT observations with short-duration moored deployments. The SPOT program [**?**]provides over two decades of full-depth hydrographic profiles, enabling characterization of stratification, seasonal variability, and interannual signals, including ENSO. In contrast, the moored ADCP deployments resolve higher-frequency processes within the bottom boundary layer, capturing tidal currents and velocity variability that are directly relevant to sediment resuspension. Together, these complementary datasets link climate-scale variability to local bottom-layer dynamics.

3.1 Flushing Events

Deep-basin flushing events in the SPB are characterized by episodic intrusions of colder, more oxygenated water that propagate over the basin's sills and intermittently ventilate the deep basin. Previous studies suggest that these events are weaker and less frequent in SPB than in the neighboring Santa Monica and Santa Barbara Basins, consistent with the greater isolation of SPB below the sill depth and its comparatively weak deep-water variability (Figure 3.1). Flushing events are typically identified by abrupt decreases in temperature, increases in dissolved oxygen, and enhanced near-bottom flow associated with overflow currents crossing the basin's sills.

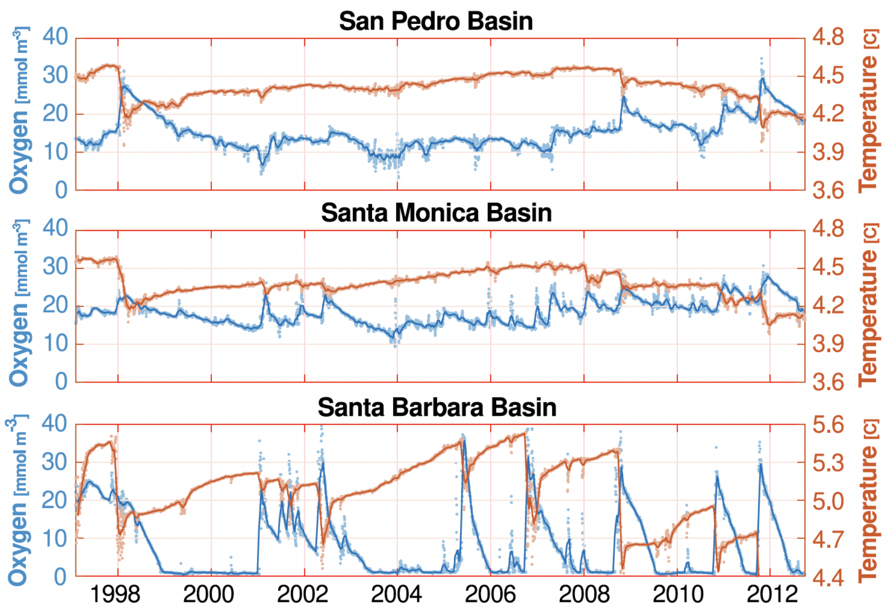

Figure 3.1. Time series of deep-basin temperature and oxygen exchange across major sill regions in the SCB, from [19]. The relatively weak variability in SPB compared to neighboring basins highlights the restricted nature of exchange below the sills. This supports the interpretation that SPB's deep water are weakly ventilated and isolated. Understanding these conditions is important for understanding the long-term preservation and limited remobilization of contaminated sediment.

During the 2023 and 2024 mooring deployments, however, no clear signatures of a major flushing event were observed in the hydrographic or velocity records, suggesting that the measurements primarily captured background tidal and subtidal variability rather than large episodic renewal events. Temperature variability observed by the near-bottom mooring was also extremely small throughout the deployment period, with only weak fluctuations around the long-term SPOT climatology and no abrupt cooling events typically associated with dense overflow intrusions or deep-basin renewal (Figure 3.2a, 3.2b).

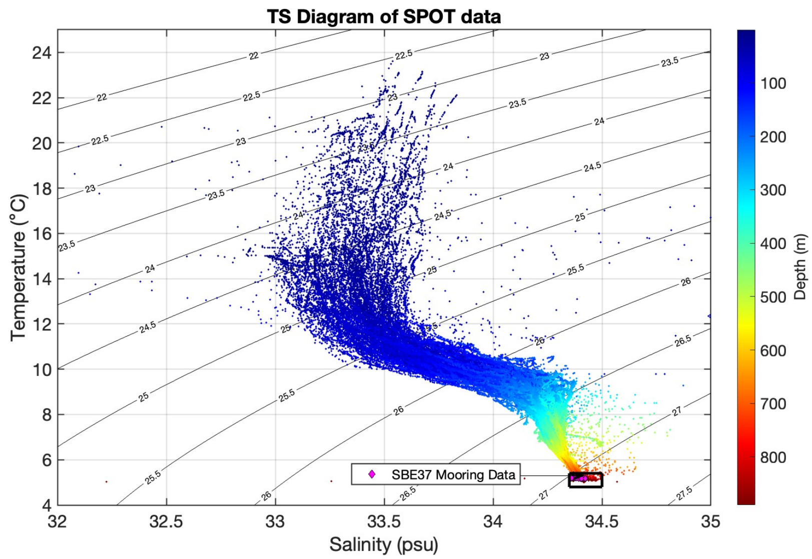

(a) TS diagram.

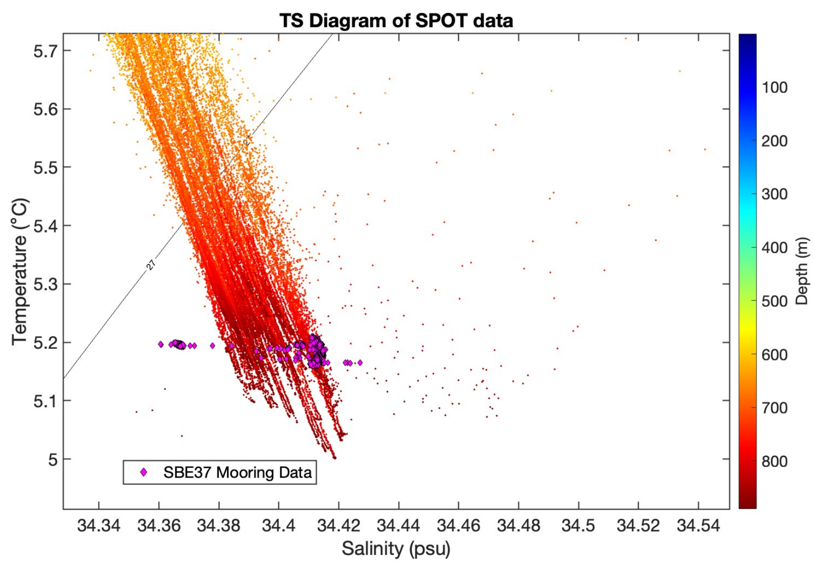

(b) TS diagram of bottom 50 m.

Figure 3.2. Temperature–salinity (T–S) diagrams for the San Pedro Basin water column. (a) Full-depth profiles illustrate the overall water mass structure, while (b) a zoom of the bottom 50 m highlights the weak thermal and salinity gradients characteristic of the isolated deep layer.

3.2 Seasonal variability

The deep water of the San Pedro Basin exhibits very limited variability in potential density (σ_0), indicating a weakly stratified bottom layer. Within the bottom 50 m of the SPOT record, σ_0 varies within approximately 0.01–0.02 kg m^{-3}, demonstrating minimal seasonal influence at depth. Summer and fall exhibit slightly higher variability compared to winter and spring, consistent with enhanced stratification in the upper water column during warmer months. However, these seasonal signals remain weak in the deep basin, reflecting the limited propagation of surface forcing into the isolated bottom layer (Figure 3.3).

Comparison with the 2024 SBE37 mooring further supports this interpretation. Observed σ_0 values during the deployment fall within approximately 0.01 kg m^{-3}, consistent with the long-term SPOT climatology and reinforcing the near-homogeneity of the bottom boundary layer (Figure 3.3).

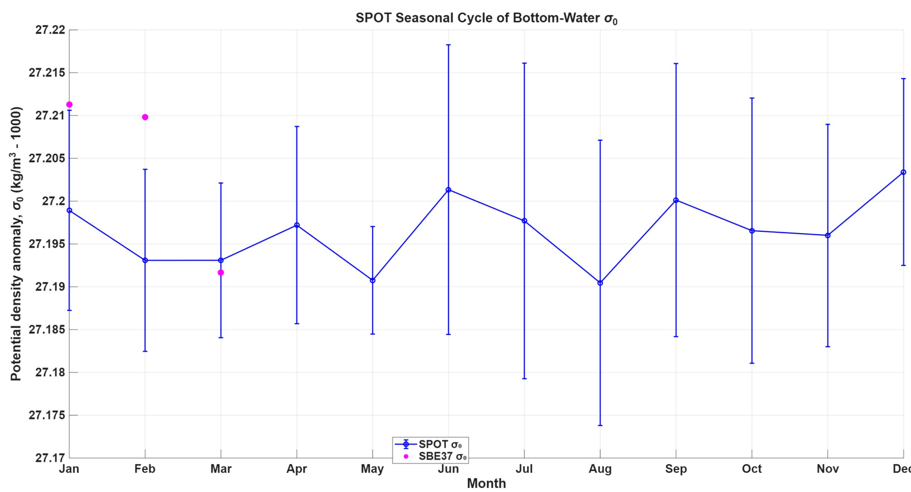

Figure 3.3. Monthly climatology of potential density (σ_0) from SPOT observations. Error bars represent the standard deviation across all years. Overlaid markers indicate corresponding measurements from the 2024 mooring deployment (SBE37), showing general agreement with the long-term seasonal cycle.

3.3 ENSO variability

Having established that seasonal variability is weak, we next examine the influence of interannual forcing through ENSO. The Niño 3 index has been hypothesized to influence deep basin variability through modulation of cross-sill pressure gradients [19]. Relationships between the Niño 3 index and both dissolved oxygen and potential density show weak correlations and substantial scatter, indicating that ENSO-related variability does not propagate strongly into the deep SPB (Figure 3.4).

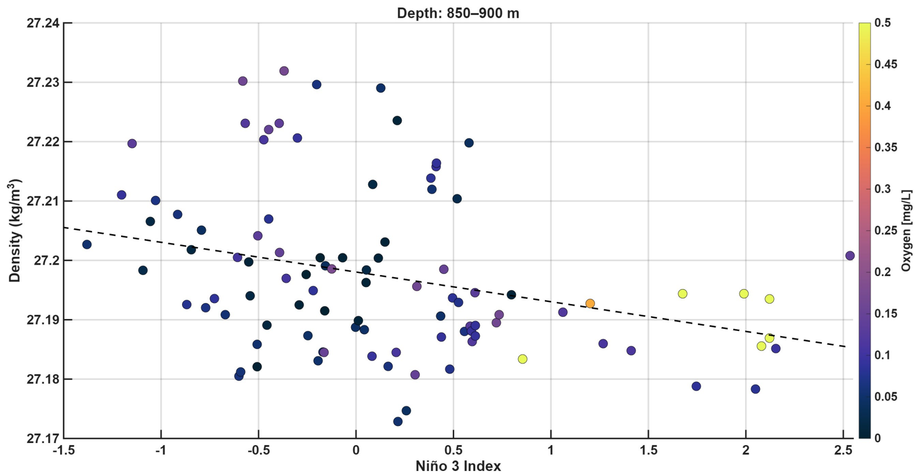

Figure 3.4. Relationship between dissolved oxygen concentrations from SPOT and the Niño 3 index in the deep San Pedro Basin (850–900 m). Data are grouped by season to assess potential seasonal variability. The large scatter and weak trend indicate minimal influence of ENSO on deep oxygen variability.

Cross-correlation between SPOT density anomalies and the Niño 3 index further confirms this result, with low coherence ($r < 0.2$). This is consistent with previous observations that renewal events occur irregularly and are not tightly synchronized with ENSO forcing. In contrast to modeled basin relaxation timescales of approximately one month [19], these results suggest that the restricted geometry of SPB dampens large-scale signals, limiting their influence on deep-water variability and renewal.

3.4 Subtidal, Inertial and Tidal Variability

We characterize near-bottom current variability in SPB using power spectral density, variance ellipses, harmonic constituent analysis, and rotary spectra. These approaches resolve the dominant frequency bands, principal flow orientation, and the relative importance of tidal and inertial forcing within the bottom boundary layer.

Power spectral density (PSD) estimates were computed using Welch's method to identify dominant tidal and inertial frequency bands within the near-bottom currents. Spectra were calculated from depth-averaged ADCP velocities, where the U and V components were averaged across all valid height-above-bottom for each time step. This produced a representative bottom-boundary-layer velocity time series while reducing variability associated with individual depth bins.

The PSD was calculated separately for the depth-averaged U and V components using MATLAB's **pwelch** function. The sampling frequency was defined from the mean ADCP sampling interval and converted to cycles per day. Spectral estimates used a window length of 22,392 samples with 50% overlap and equivalent FFT length to improve the statistical stability of the spectral estimates. Frequencies are reported in cycles per day, and the main diurnal and semidiurnal constituents, along with the theoretical local inertial frequency, were marked for comparison with the observed spectral peaks.

The depth averaged mean flow is u_m = -0.92cm/s and v_m = -0.54cm/s. The dominant energy peaks occur at the semidiurnal tidal constituents M2 ($\sim$1.93 cpd) and S2 ($\sim$2.00 cpd), indicating that semidiurnal tidal forcing dominates near-bottom current variability in SPB (Figure 3.5). This suggests that bottom currents are primarily driven by predictable oscillatory tidal motions rather than stochastic or low-frequency processes. Secondary energy is present at diurnal and near-inertial frequencies, but these contributions are weaker relative to the semidiurnal band.

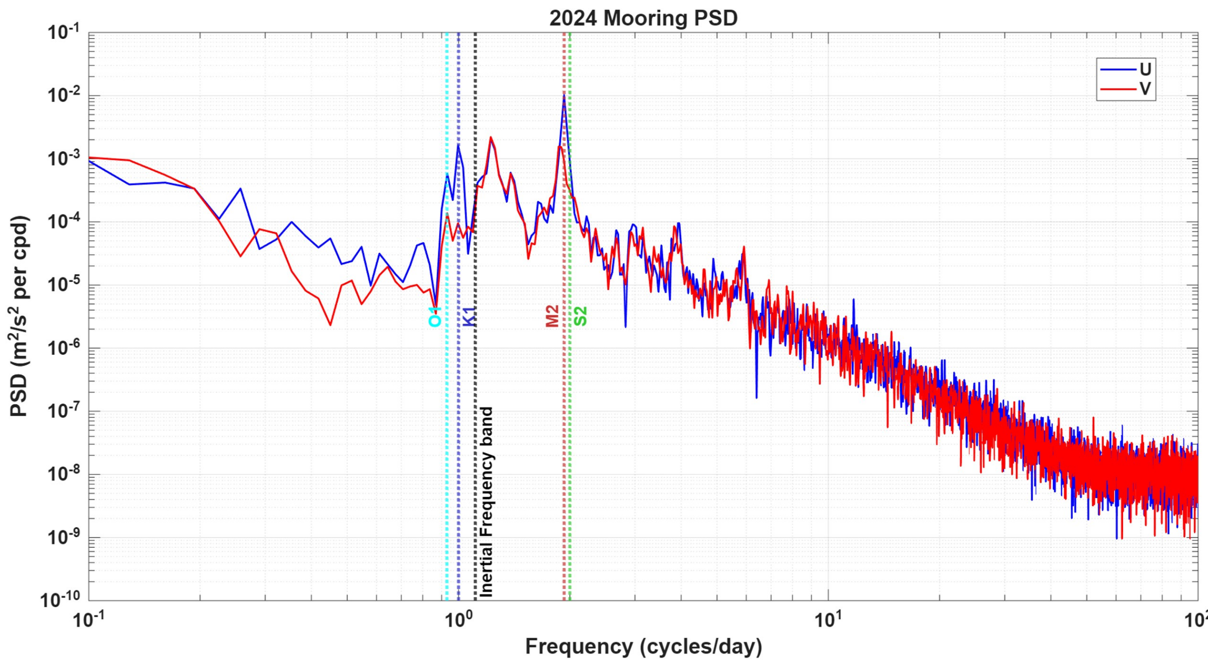

Figure 3.5. Power spectral density of depth-averaged U and V currents from the 2024 ADCP mooring deployment. Peaks at diurnal and semidiurnal frequencies indicate dominant tidal forcing, with additional energy near the inertial frequency.

While the PSD identifies which tidal constituent dominates the energetics of the flow in the center of SPB, the variability in directionality cannot be observed in this analysis. To examine the structure of the horizontal flow, we compare the joint distribution of the U and V velocities with the tidal constituent ellipses derived from the ADCP record.

To further characterize the directional structure of the near-bottom flow, variance ellipses and two-dimensional velocity distributions were computed from the depth-averaged horizontal currents. Variance ellipses were derived from the covariance matrix of the depth-averaged U and V components using eigenvector decomposition, providing estimates of the principal axes and directional variability of the flow field. Two-dimensional histograms of the U and V currents were additionally used to visualize the distribution of the horizontal velocities throughout the deployment (Figure 3.6).

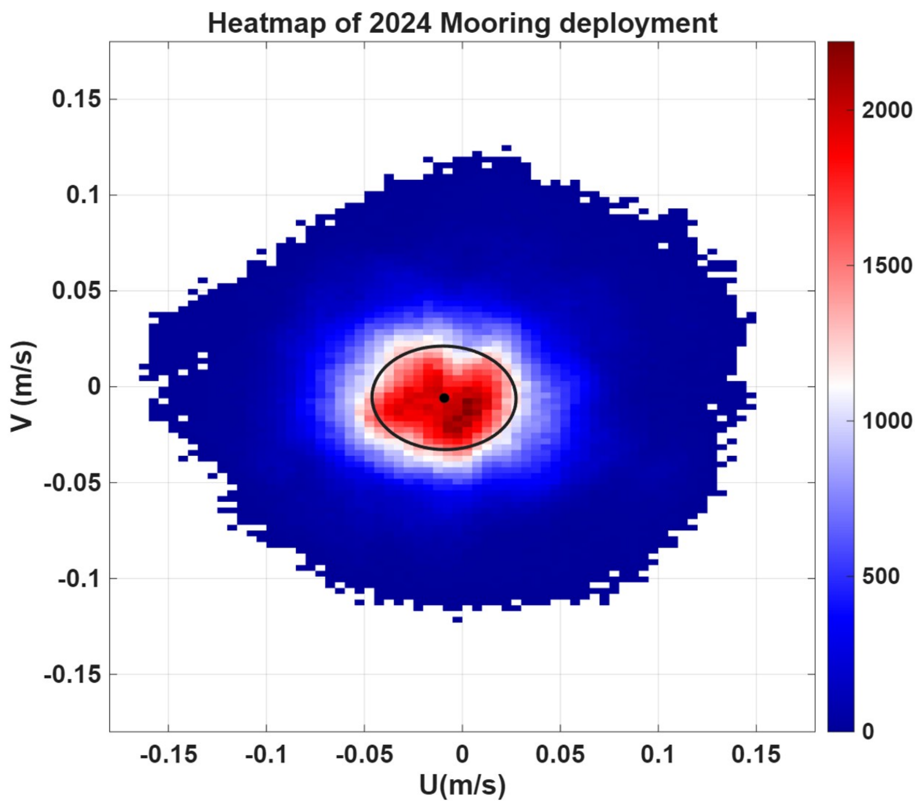

Figure 3.6. Two-dimensional histogram (heatmap) of horizontal current velocities (U and V) from the 2024 mooring deployment. Color shading represents the frequency of occurrence, with warmer colors indicating more frequent velocities. The elliptical structure highlights the dominant flow variability and directional spread.

The velocity distribution is centered near zero, indicating that most of the observed currents are relatively weak and oscillatory rather than continuously directed. Variability is slightly greater in the U component than in the V, but distribution is broadly symmetric. This suggests that the near-bottom flow is dominated by the back-and-forth oscillating motion rather than a strong mean current.

Harmonic tidal analysis was performed on the depth-averaged velocity field using the MATLAB package t_tide. The U and V velocity components were combined into a complex velocity field

$$u + iv \tag{3.1}$$

allowing decomposition into the dominant tidal constituents and their associated ellipse parameters. The major diurnal and semidiurnal constituents were analyzed (M2, S2, K1, and O1). Tidal ellipse parameters, including major and minor axes and inclination, were extracted from the harmonic outputs and used to reconstruct the directional structure of the oscillatory flow in the U-V velocity space.

The tidal ellipses provide a constituent-based view of the aforementioned variability (Figure 3.7). The dominant semidiurnal constituent (M2) has the largest tidal ellipse, supporting the PSD result that M2 is the primary contributor to the near-bottom flow. This consistency across spectral and directional analyses indicates that near-bottom variability in SPB is primarily driven by predictable tidal forcing, rather than sustained mean flow or episodic directional currents.

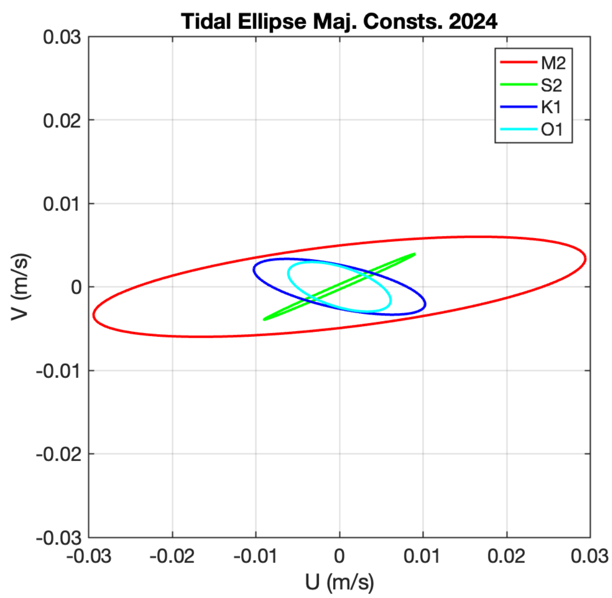

Figure 3.7. Tidal current ellipses for the dominant constituents derived from the 2024 ADCP data. Ellipse orientation and magnitude illustrate the directional structure and strength of tidal currents in the deep San Pedro Basin.

While the tidal ellipses describe the amplitude and orientation of the dominant constituents, they do not distinguish between clockwise and counterclockwise rotational components of the flow. To further resolve the structure of the velocity field, we examine the rotary spectra of the depth-averaged currents.

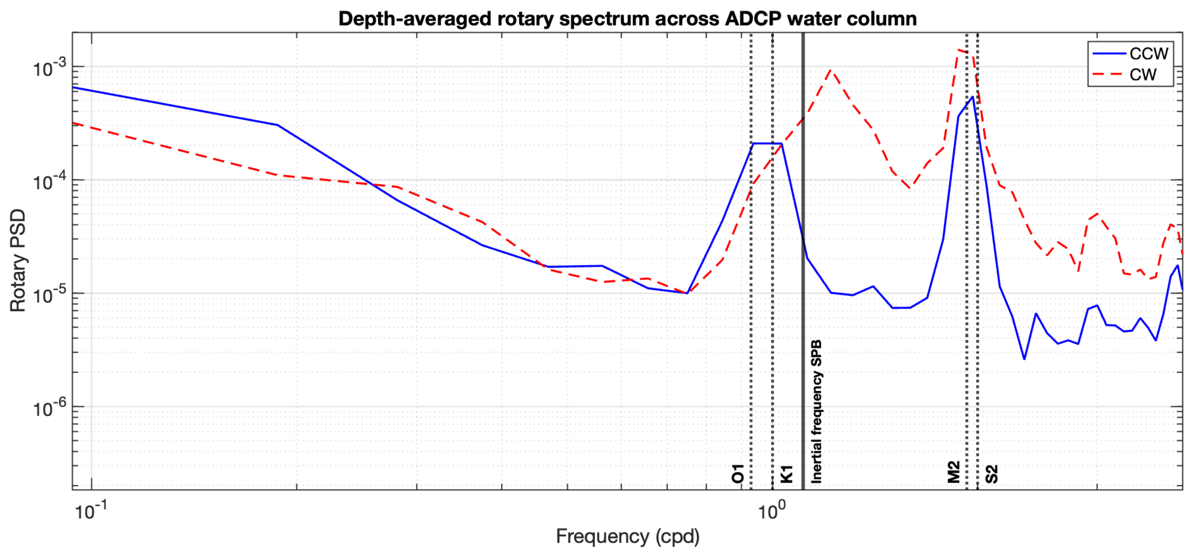

Figure 3.8. Rotary spectra of depth-averaged ADCP currents. Clockwise and counterclockwise components highlight energy partitioning, with peaks at tidal and near-inertial frequencies indicating dominant forcing mechanisms.

The rotary spectra show energy distributed between clockwise (CW) and counterclockwise (CCW) components, with peaks at semidiurnal tidal frequencies and weaker energy peaks near the inertial band and diurnal frequencies (Figure 3.8). Energy is concentrated in the CW component, consistent with expectations for motions near the inertial frequency in the Northern Hemisphere. This distribution is consistent with the dominance of oscillatory tidal forcing identified in the PSD.

The rotary spectra exhibit elevated energy near the local inertial frequency, although the spectral peak is shifted from the canonical Coriolis frequency. In the presence of background relative vorticity, the effective inertial frequency is modified as

$$f_{eff} = f + \frac{\zeta}{2} \tag{3.2}$$

where f is the Coriolis parameter and ζ is the vertical relative vorticity. At the latitude of SPB (~33.5°N), the theoretical inertial frequency is approximately $f \approx 1.11$ cpd. However, the observed spectral peak occurs closer to $f_{eff} \approx 1.22$ cpd, corresponding to an approximate 10%

increase relative to the canonical inertial frequency. This shift is consistent with the modification of the effective inertial frequency by background relative vorticity or basin-scale circulation within SPB.

Overall, observations from SPOT and the near-bottom mooring deployments indicate that the deep San Pedro Basin is characterized by weak stratification, limited seasonal and interannual variability, and relatively infrequent deep-water renewal. Variability within the bottom layer is dominated primarily by semidiurnal tidal forcing, with weaker contributions from subtidal and inertial motions, while no clear flushing events were observed during the 2023 and 2024 deployments. These results suggest that the deep basin remained in a relatively quiescent state during the observational period, providing an opportunity to examine the structure and dynamics of the bottom boundary layer under typical background conditions.

Chapter 4

Sediment Resuspension Events

The structure and dynamics of the bottom boundary layer play a critical role in determining whether contaminated sediments within the San Pedro Basin remain buried or become remobilized. Although previous chapters demonstrated that deep SPB circulation is generally weak and dominated by oscillatory tidal forcing, even intermittent increases in near-bottom shear stress may influence sediment transport, benthic mixing, and contaminant exposure at the seafloor. In this chapter, we examine the vertical structure and variability of near-bottom currents using moored ADCP observations and empirical orthogonal function (EOF) analysis to characterize the dominant modes of bottom boundary layer variability. These observations are then used to estimate bed shear stress and evaluate whether observed hydrodynamic conditions are sufficient to exceed theoretical and empirical erosion thresholds for cohesive SPB sediments.

4.1 Bottom Boundary Layer Structure

To examine how the vertical structure of the horizontal currents within the 38 meters, we employed an EOF. EOF's decomposition separates the velocity fields into orthogonal vertical modes, allowing identification of the dominant coherent structure and higher order variability within the bottom boundary layer. EOF analysis was applied to the vertical current structure to isolate the dominant coherent modes of variability within the bottom boundary layer (Figure 4.1). EOF modes were computed using singular value decomposition (SVD) of the U and V velocity fields:

$$X = USV^T \tag{4.1}$$

where the columns of U represent the orthogonal spatial modes, S contains the singular values, and the temporal variability associated with each mode is represented by the columns of V scaled by the singular values. The percent variance explained by each EOF mode was calculated from the squared singular values normalized by the total variance.

The leading mode (mode 1) shows a near-linear vertical structure for both U and V currents, indicating that the dominant variability is coherent with depth and maintains a consistent flow direction across the bottom boundary layer (Figure 4.1). This indicates that the flow is not composed of opposing turbulent layers, but rather a vertically uniform response. The amplitude of mode 1 increases slightly with height above the bottom, consistent with the influence of bottom friction, which reduced velocities near the seabed. The second mode (mode 2) contains a single zero crossing, showcasing a higher-order structure associated with vertical shear and oscillatory variability. Together, these modes suggest that the near-bottom currents are mostly coherent, tidally driven, with secondary variability from shear arising in the boundary layer.

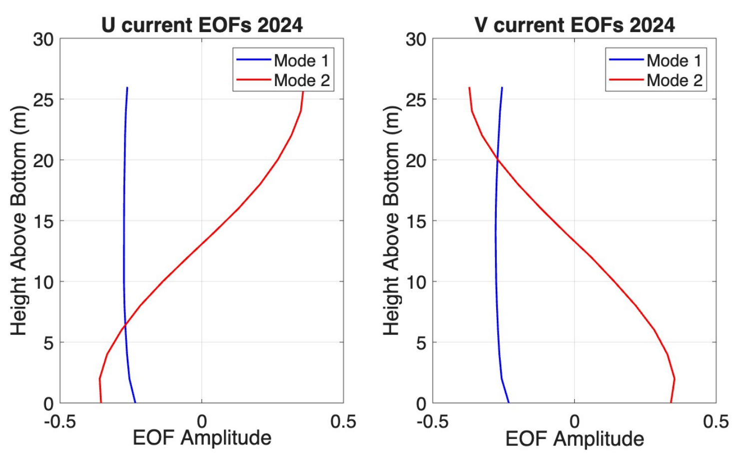

Figure 4.1. Vertical structure of the leading EOF modes for the horizontal currents. The left panel shows the U (east–west) component, and the right panel shows the V (north–south) component. The dominant mode captures the primary depth-dependent structure of the flow in the lower water column.

The percent variance explained by each EOF mode shows that the leading mode (mode 1) accounts for 95.5% and 92.2% of variance for U and V, respectively (Figure 4.2). Higher order modes contribute a significantly smaller fraction of total variance, with mode 2 accounting for less than 5%, and all remaining modes collectively negligible. This reinforces that bottom boundary layer variability in SPB is low-dimensional and largely controlled by a single, tidally forced mode.

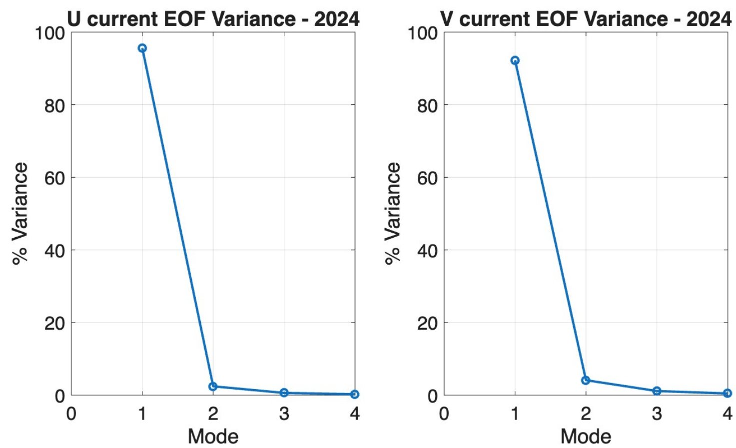

Figure 4.2. Percent variance explained by empirical orthogonal function (EOF) modes for U and V currents from the 2024 mooring deployment. The first mode captures the majority of variance, indicating a dominant flow structure.

Reconstruction of the velocity fields using the first two EOF modes (Figure 4.3) isolates the dominant coherent variability within the bottom boundary layer from higher-order residual fluctuations (Figure 4.4). Because the leading EOF modes account for the majority of the variance in the velocity field, the reconstructed currents primarily capture the large-scale oscillatory structure associated with tidal and near-inertial motions. In contrast, the residual anomaly fields highlight weaker, intermittent, and vertically incoherent variability not represented by the dominant modes, including localized shear and smaller-scale transient fluctuations.

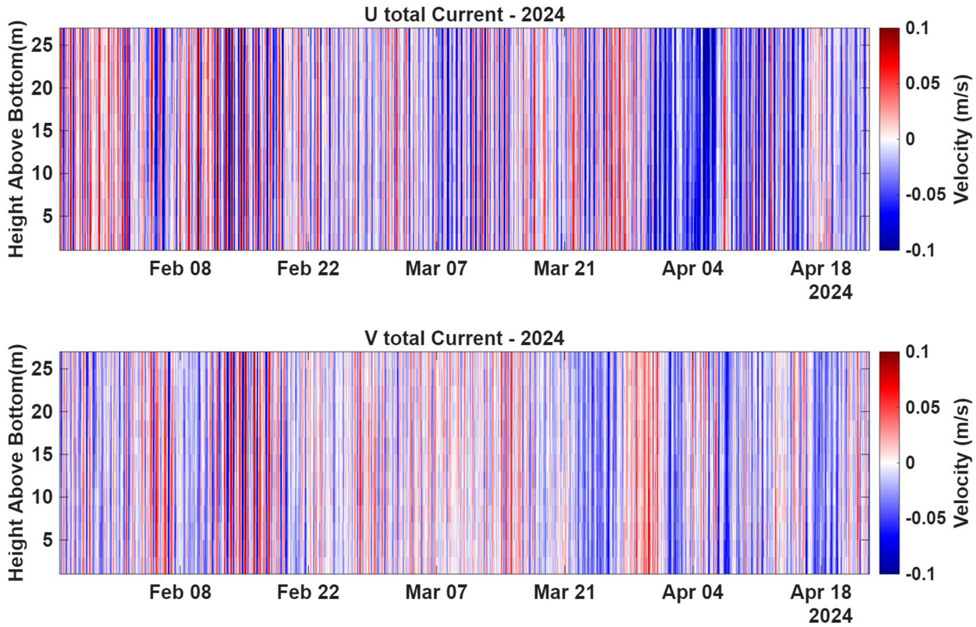

Figure 4.3. Time–depth evolution of horizontal currents (U and V) from the 2024 mooring deployment. Color shading represents velocity magnitude, highlighting temporal variability and depth structure in the flow field.

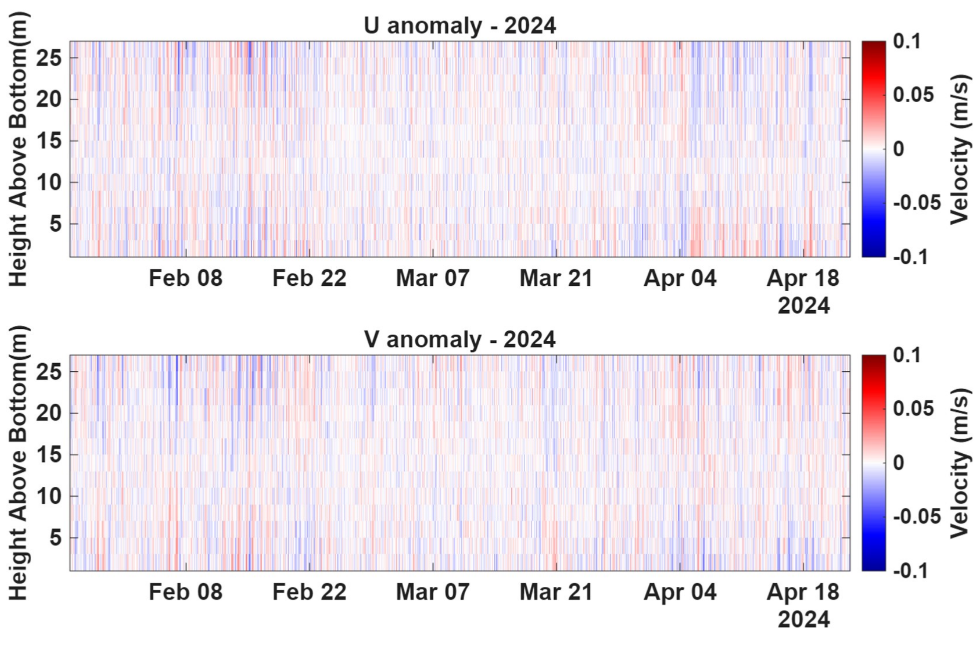

Figure 4.4. Time–depth evolution of current anomalies (U and V) from the 2024 mooring deployment after removal of the mean. Anomalies emphasize variability associated with tidal and subtidal processes.

4.2 Resuspension Events

Bed shear stress is the primary driver of resuspension and erosion. Resuspension occurs when the applied bed shear stress exceeds the critical shear stress required for mobilization. Near-bottom ADCP velocities from the mooring deployment were used to estimate the magnitude and temporal variability of bed shear stress within the bottom boundary layer. Initially, my approach was to assume a logarithmic boundary layer and employ

$$u(z) = \frac{u_*}{\kappa} \ln\left(\frac{z}{z_0}\right), \tag{4.2}$$

where u_* is the friction velocity, $\kappa \approx 0.4$ is the von Kármán constant and z_0 is the roughness length. Log-law fitting assumes that there is a turbulent logarithmic boundary layer, vertically coherent shear profiles, and a representative z_0. The applicability of the logarithmic boundary layer assumption was evaluated through quality control filtering because the observed near-bottom currents were frequently weak and variable. Using the goodness-of-fit metrics, only 4.95% of the profiles satisfied the fitting criteria, illustrating that the observed flow did not exhibit a clear logarithmic boundary layer structure. Due to the low number of accepted fits, a drag-law formulation was adopted as the primary estimate of bed shear stress.

$$\tau_b = \rho C_D U^2 \tag{4.3}$$

where C_d is the drag coefficient, and ρ is the density of seawater. The representative near-bottom velocity was calculated using the horizontal current magnitude at 2 m HAB.

$$U = \sqrt{u^2 + v^2} \tag{4.4}$$

The 2 m HAB bin was selected because ADCP velocity measurements were resolved in 2 m vertical increments. Choosing the 2 m bin avoids interference and increased uncertainty associated with the lowest near-bed velocity bins, and is still close enough to estimate the near-bed forcing and representative near-bed free-stream velocity. The drag coefficient C_d =0.0025 was taken from the U.S. Navy Hybrid Coordinate Ocean Model, and is widely used for deep-sea shear estimates. The drag-law framework provides a stable first-order estimate of applied bed stress under weak flow conditions, allowing τ_b to be compared against critical erosion thresholds.

To evaluate whether the observed shear stresses were sufficient to mobilize the sediment, the estimated τ_b values were compared against theoretical and empirical erosion thresholds. The initial framework employed for this comparison was the Shields parameter, a dimensionless measure of the fluid stress acting on a sediment grain relative to its submerged weight. It is defined as

$$\theta = \frac{\tau_b}{(\rho_s - \rho) g D} \tag{4.5}$$

where τ_b is the bed shear stress, ρ_s is sediment density, ρ is fluid density, g is gravitational acceleration, and D is a representative grain diameter (typically D_{50}). The Shields parameter is most commonly applied to noncohesive sediment and hydraulically rough sandy beds. However, the sediments in the central SPB are predominantly cohesive fine-grained silts and clays [10], with mean grain sizes of 4–8 μm and upper ranges reaching 63 μm. Under these conditions, the Shields framework becomes highly sensitive to grain size and less representative of cohesive sediment behavior.

Due to the cohesive nature of the sediments in SPB, empirical cohesive erosion relationships were adopted for the analysis. Cohesive sediments are primarily fine-grained heterogeneous aggregates held together via electrochemical forces[4]. The porous nature of cohesive sediment influences consolidation, water content, and interparticle cohesion, all of which strongly affect resistance to erosion and entrainment behavior. Under these conditions, grain size alone becomes insufficient to fully characterize sediment remobilization. Instead, dry-bulk density, defined as the mass divided by the total volume of the wet sediment sample, provides a more representative proxy for sediment strength and consolidation state. Therefore, the critical shear stress required for cohesive erosion was estimated using the empirical relationship

$$\tau_{cr} = \alpha \rho_d^{\beta} \tag{4.6}$$

where ρ_d is the dry-bulk density, ranging from approximately 165 to 330 $\frac{kg}{m^3}$ for SPB sediments [10], α and β are empirical coefficients derived from the cohesive erosion studies of Owen (1975), Liu (2002), and Perera and Wu (2016) [28, 31, 7]. Multiple empirical coefficients were evaluated in order to assess the sensitivity of the cohesive erosion thresholds of similar sediment types to the sediment of SPB.

The dry-bulk densities selected for this analysis represent the range reported for SPB sediments [10]. However, sediment cores collected from nearby, but shallower, Palos Verdes Shelf have reported substantially higher dry bulk densities [8, 29], reflecting the broader consolidation states within the SCB. Although these sediments are not directly comparable to the deep-basin deposits of SPB, they demonstrate that a broader range of physical sediment properties exists within contaminated sediments of the Southern California Bight and highlight the sensitivity of cohesive erosion thresholds to assumptions regarding sediment consolidation.

The near-bottom velocities at 2 m HAB were generally weak throughout the 2024 mooring deployment, with intermittent periods of enhanced flow. The maximum U and V were 0.107 and 0.085 $\frac{m}{s}$ respectively, while the median velocities were 0.01 and 0.0075 $\frac{m}{s}$ respectively (Figure 4.5). The horizontal speed shows a maximum of 0.124 $\frac{m}{s}$ and a median speed of 0.038 $\frac{m}{s}$. The median U and V velocities remained near zero throughout the deployment, indicating that the near-bottom flow was primarily oscillatory rather than characterized by a persistent unidirectional current.

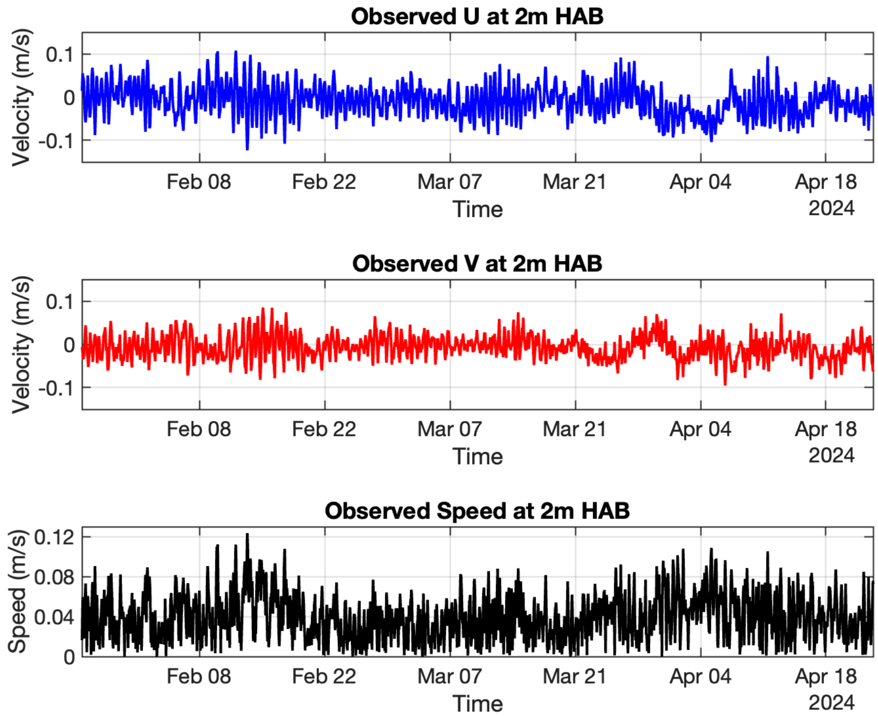

Figure 4.5. Time series of horizontal velocities and total current speed measured at 2 m HAB during the 2024 mooring deployment. The upper two panels show the east-west (U), and north-south (V) velocity components, while the bottom panel shows the horizontal current speed. Near-bottom currents are generally weak, with typical velocities below 0.1 $\frac{m}{s}$, and exhibit oscillatory variability consistent with strong tidal influence in the boundary layer.

The bed shear stress is low overall at 2 m HAB, with maximum τ_b reaching 0.039 Pascals (Pa) (Figure 4.6), and a median value of 0.0038 Pa. The peaks in the shear stress are episodic, highlighting the oscillatory flow of SPB bottom boundary layer currents, with a clear tidal signal visible across the time series

Applying the Shields framework for noncohesive sandy sediment to the calculated τ_b values indicates that some exceedance events are possible during periods of enhanced near-bottom flow (Figure 4.6). However, as discussed previously, the Shields framework is most appropriate for unconsolidated sandy beds and becomes highly sensitive to grain size at very small particle diameters. This approach is therefore less representative of the cohesive, consolidated silty muds that dominate the sediments within SPB.

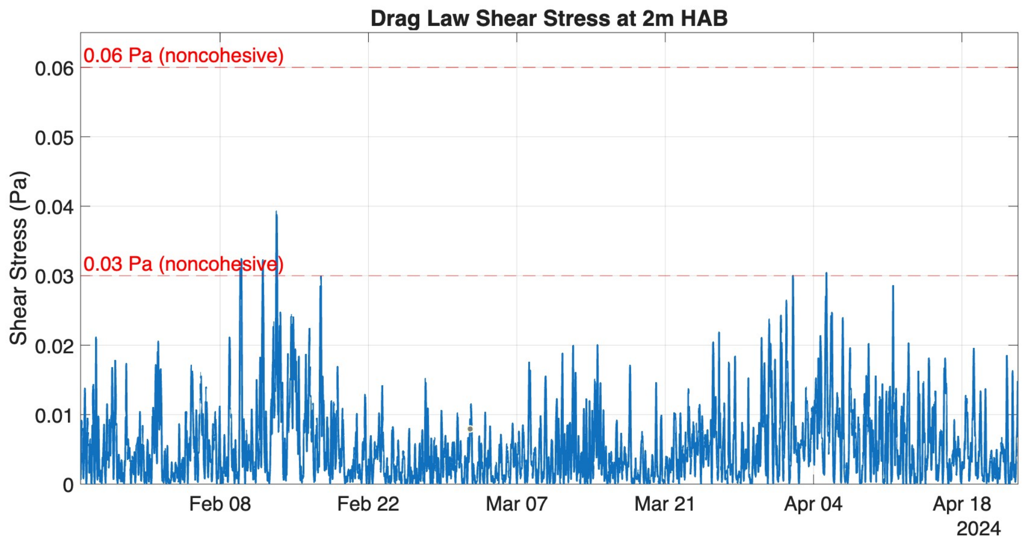

Figure 4.6. Time series of bed shear stress estimated using the drag-law formulation at 2 m HAB from the 2024 ADCP mooring deployment. Horizontal lines represent critical Shields-based erosion thresholds calculated for representative representative grain sizes of 4 μm, 8 μm, and 63 μm. These thresholds are most applicable to loose sandy beds, such as unconsolidated and noncohesive beach sand, and only provide a first-order comparison between observed shear stress and theoretical sediment entrainment conditions as our expectation of the sediments at the study site is dominated by silt.

Because the seafloor of SPB is dominated by cohesive silty mud rather than unconsolidated sand, the drag-law shear stress estimates were also compared to a set of empirical cohesive thresholds. This comparison allows for a more reflective test of whether the observed flow across the bed was capable of remobilization.

Comparing the observed τ_b with the empirical thresholds from Owen, Liu, and Perera & Wu [28, 31, 7], the estimated bed shear stress remains below even the lowest cohesive threshold across the entire time series (Figure 4.7). Intermittent increases in the 2 m HAB velocity produce peaks in τ_b; the stresses generated aren't large enough to exceed the resuspension thresholds. This indicates that under the observed conditions in 2024, shear-driven resuspension of the SPB sediment is unlikely. The logarithmic y-axis highlights the large dynamic range in the observed bed shear stress and emphasizes the quiescent nature of the boundary layer. Even during the strongest velocity events, the bed stress generated remains under the critical thresholds.

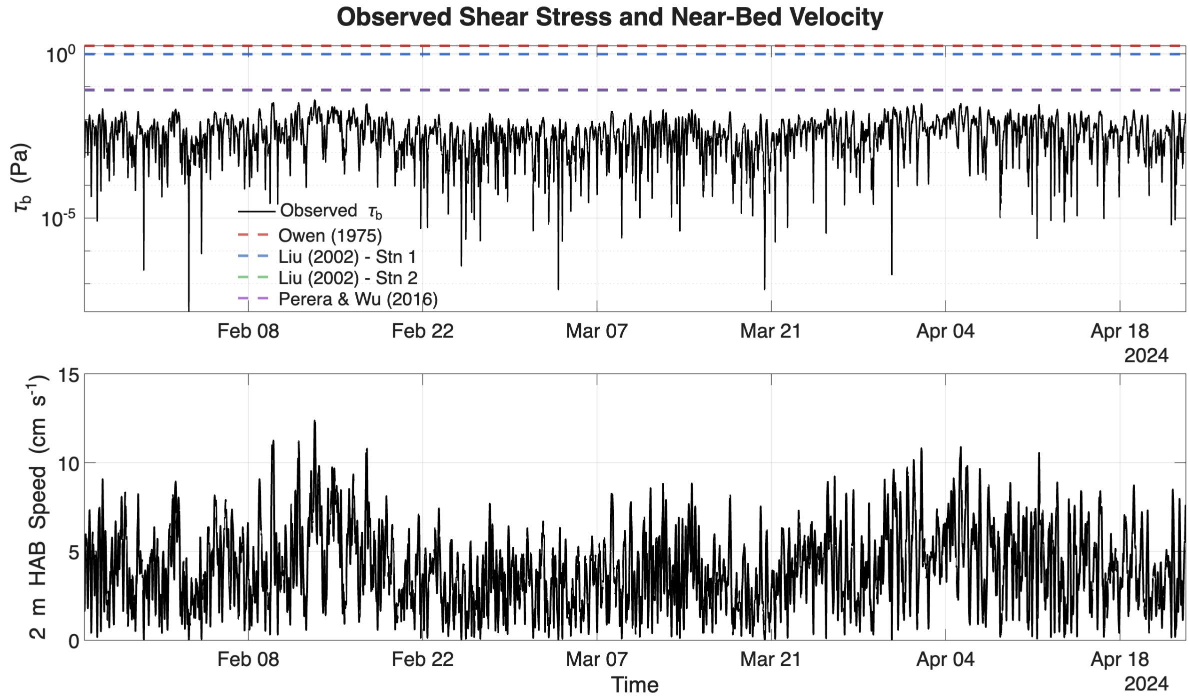

Figure 4.7. Upper panel: Time series of estimated bed shear stress (τ_b) calculated using the quadratic drag-law approach from observed horizontal current speeds at 2 m HAB. Dashed horizontal lines indicate empirical critical shear stress thresholds for cohesive sediment erosion [1]. Observed τ_b values remain consistently below all modeled cohesive erosion thresholds throughout the deployment. Lower Panel: Corresponding near-bed current speed at 2 m HAB used in the drag-law calculation. Although episodic increases in flow speed are observed, they are insufficient to generate bed stresses capable of initiating widespread cohesive sediment resuspension.

The resulting critical velocity curves demonstrate that the flow required for resuspension varies greatly depending on both the empirical formulation and assumed drag coefficient (Figure 4.8). Higher drag coefficients reduce the critical velocity necessary for erosion, as greater momentum transfer to the bed produces larger bed shear stress for the same near-bottom flow. Across all formulations, the higher dry-bulk density case ($\rho_d = 330\frac{kg}{m^3}$) requires a substantially larger critical velocity than the lower density case, reflecting the greater resistance of more consolidated sediment to erosion.

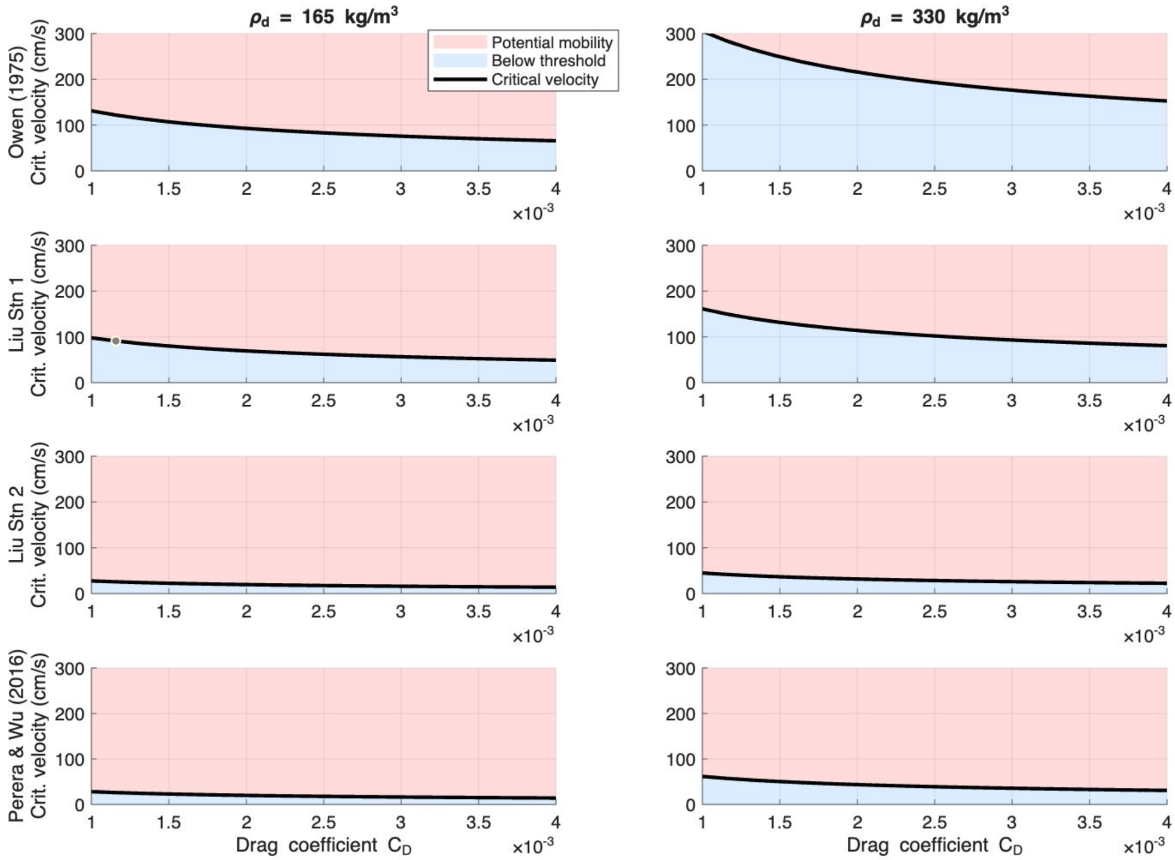

Figure 4.8. Critical velocity required to exceed modeled cohesive sediment erosion thresholds as a function of drag coefficient C_D for two representative dry-bulk densities observed in SPB sediments ($\rho_d = 165$ and $\rho_d = 330\ \frac{kg}{m^3}$). Rows correspond to empirical formulations from Owens (1975), Liu et al (2002) stations 1 and 2, and Perera & Wu (2016). The black line is the critical velocity required to initiate erosion for each formulation. The shaded regions indicate conditions below threshold (blue) and potential mobility (red). Required critical velocities generally exceed observed near-bottom currents, particularly for higher density consolidated, supporting the interpretation that the hydrodynamic conditions in SPB are insufficient for widespread sediment erosion.

The Owens (1975) and Liu station 1 produce the highest critical velocities, often exceeding 50 - 150 $\frac{cm}{s}$ across the drag coefficient range, which is substantially larger than the observed near-bottom currents in SPB. In contrast, Liu station 2 and Perera & Wu (2016) formulations yield lower thresholds($\approx$ 15-60 $\frac{cm}{s}$), indicating that even the most energetic flow could potentially approach conditions of resuspension.

Chapter 5

Seafloor Imagery

The persistence of DDT and DDX within SPB sediments raises important questions regarding long-term contaminant burial, sediment remobilization, and potential pathways into the deep marine ecosystem. While previous studies have mapped widespread contamination throughout the basin, less attention has been given to the relationship between contaminated sediments and benthic biological activity at the seafloor. In this chapter, sediment core observations are combined with seafloor imagery to examine the spatial distribution of DDT contamination, characterize burial depth and concentration patterns, and investigate whether visible benthic communities or biological activity may provide mechanisms for contaminant interaction with the surrounding marine food web.

5.1 Sediment Cores

We used 54 sediment core samples from [22, 30] to quantify and map the spatial and depth extent of DDT and DDX. The analysis quantifies the depth of burial across the basin, as well as the areas of highest concentration of DDT and DDX(μg/kg). The cores are distributed throughout the basin, with the highest density of cores transecting the basin from the Palos Verde shelf to the northeast coast of Santa Catalina Island (Figure 5.1). A large fraction of cores is located within DS2, allowing a more robust analysis of the sediments in the area of our mooring data.

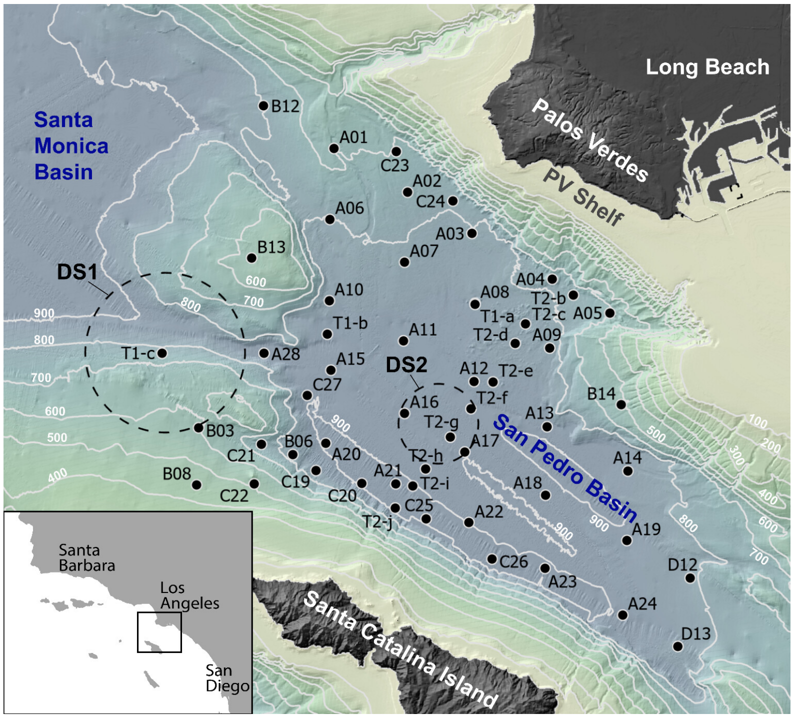

Figure 5.1. Bathymetric map of the San Pedro Basin showing the locations of 54 sediment cores. Color shading and contour lines represent seafloor depth, while dashed circles indicate the primary ocean disposal sites (DS1 and DS2). The inset provides regional context within the Southern California Bight. Reproduced from [30]

Natural neighbor interpolation was applied to estimate and resolve spatial patterns in DDT and DDX concentrations between core locations (Figure 5.2). This method generates a continuous surface constrained by the irregularly spaced observations, providing reasonable estimates in regions not directly sampled. The interpolated fields reveal a clear spatial structure in both the depth of maximum DDT concentration and the magnitude of the DDT and DDX hotspots. Maximum burial depths are highest along the continental slope, where enhanced sediment accumulation—driven by terrigenous input from the Palos Verdes shelf and lithogenic contributions from runoff—promotes deeper sequestration of contaminants [25]. In contrast, high-concentration hotspots are more spatially variable, with peak DDT and DDX values occurring along the shelf and extending into the basin interior. This distribution suggests a combination of downslope transport from the Palos Verdes shelf and heterogeneous disposal mechanisms, including containerized waste dumping and industrial outfall discharge [15, 20].

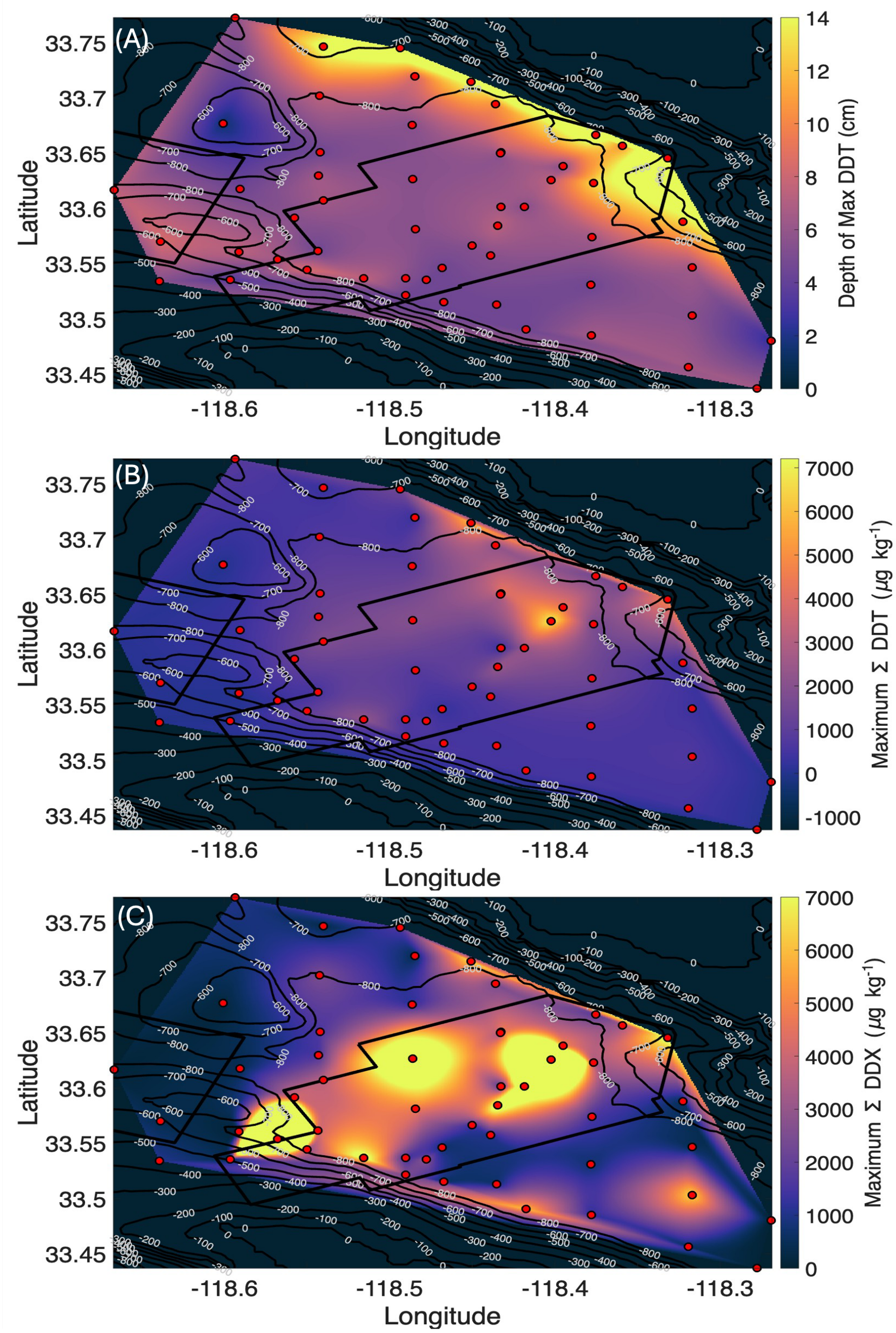

Figure 5.2. Interpolated spatial distributions of sediment core-derived properties across the San Pedro Basin: (A) Depth of maximum DDT concentration (cm), (B) maximum ΣDDT concentration at depth, and (C) maximum ΣDDX concentration. Color shading indicates magnitude, and red markers denote core sampling locations. Bathymetric contours are overlaid at 100 m intervals for geomorphic context.

Three cores around and within DS2 were selected for detailed analysis, spanning approximately 16 km across distinct depositional settings (Figure 5.3). Each core exhibits clear differences in DDT and DDX concentrations and the depth of maximum burial. Together, these records highlight the spatial variability in contaminant distribution and preservation throughout SPB.

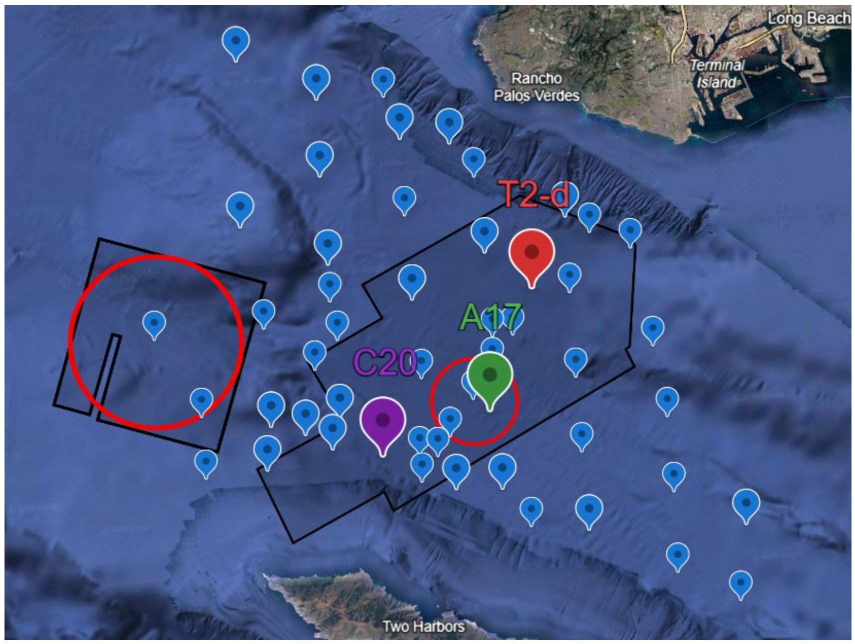

Figure 5.3. Locations of three representative sediment cores selected for detailed analysis. These cores span regions of varying DDT accumulation and sedimentary environments, allowing for comparison of contaminant penetration and vertical structure across the basin.

The vertical profiles show clear differences in both the magnitude and depth of peak DDT and DDX concentrations across the three cores (Figure 5.4). In all cores, ΣDDT and ΣDDX exhibit subsurface maxima centered between ∼5–10 cm depth. Core T2-d exhibits the highest overall concentrations, reaching 7,270 μg /kg for DDT and 32,780 μg/kg for DDX. Core C20 exhibits broader, more gradually varying profiles with depth, with the ΣDDX peak occurring approximately 2 cm deeper than the ΣDDT. In contrast, A17 exhibits the lowest concentrations and a shallower peak, suggesting reduced accumulation or enhanced dilution at this location. The variability in both peak depth and magnitude across relatively short spatial scales highlights the heterogeneous nature of DDT deposition and burial within the San Pedro Basin.

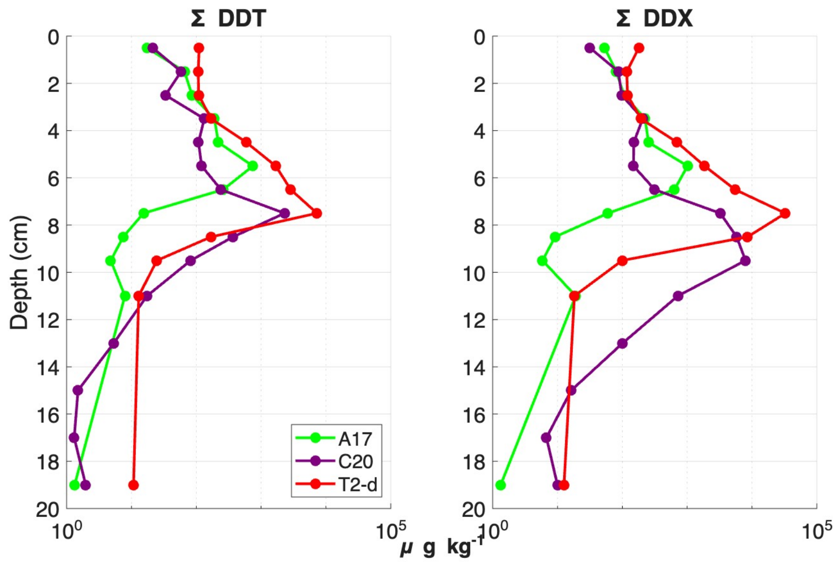

Figure 5.4. Vertical profiles of ΣDDT and ΣDDX concentrations for three selected sediment cores plotted as a function of sediment depth. All cores exhibit subsurface concentration maxima at approximately 5–10 cm. Differences in peak magnitude and depth between cores are evident, with T2-d showing the highest concentrations and A17 the lowest.

5.2 Acoustic and Optical Imagery

Seafloor imagery collected with the AUV and ROV around these core sample locations is shown in Figure 5.5. The sediment core and seafloor imagery collectively suggest that much of the SPB seafloor within and around DS2 is characterized by fine-grained sediment, with limited evidence of persistent physical disturbance. The SAS and optical imagery shown in figure 5.5 were collected during ROV surveys conducted in proximity to the sediment coring sites. Cores A17, C20, and T2-d were located within approximately 0.1–0.45 km of the selected ROV images, allowing for the imagery to provide representative seafloor conditions for each sediment sample. HISAS imagery was collected at a range of 72 m, 158 m, and 88 m for cores A17, C20, and T2-d, respectively. The proximity between the ROV surveys and core locations enables direct comparison between observed seafloor morphology and the burial depth and vertical distribution of DDT and DDX within the sediments. Across all sites, the imagery reveals predominantly low acoustic backscatter and minimal small-scale roughness, consistent with a smooth, fine-grained sediment cover (Figure 5.5). The absence of discernible bedforms or erosional features suggests limited near-bed shear stress and weak sediment mobilization. The preservation of distinct subsurface DDT and DDX concentration maxima across the basin further suggests that widespread sediment resuspension and vertical mixing remain limited under present-day hydrodynamic conditions. However, because many of the concentration maxima occur within the upper ∼5–10 cm of sediment, localized burrowing, sediment turnover, or benthic feeding activity could contribute to intermittent disturbance and exposure of contaminated material at the sediment-water interface.

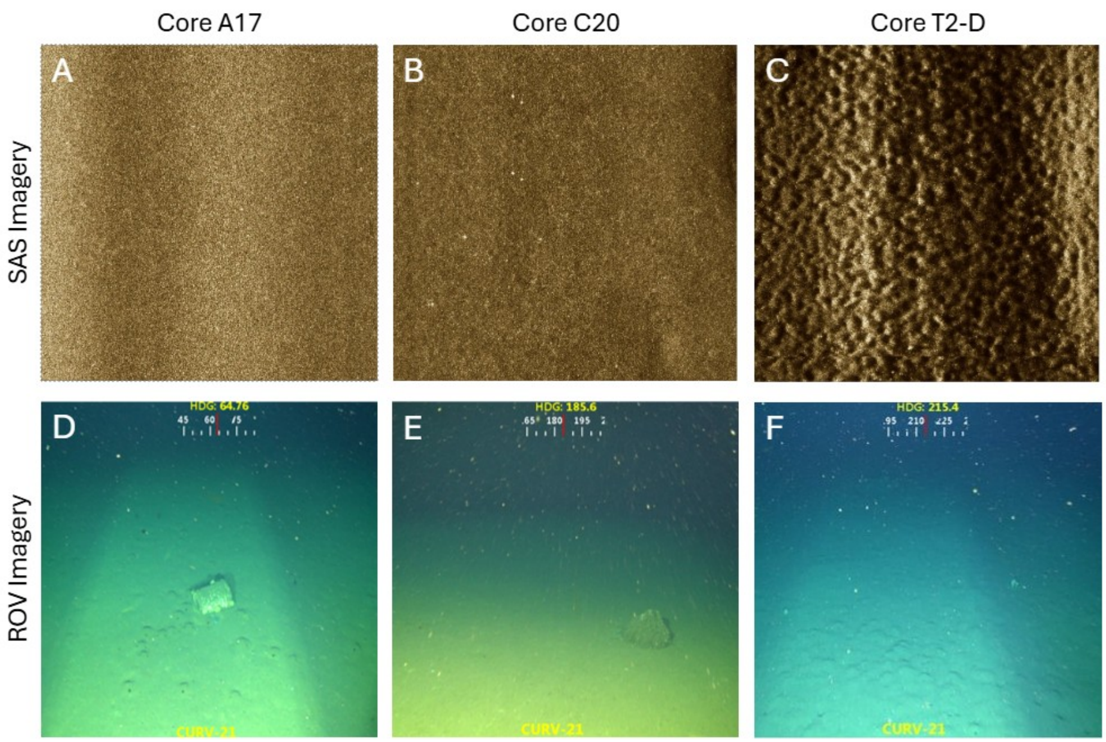

Figure 5.5. Representative SAS imagery(A-C) of the San Pedro Basin seafloor. The vehicle operated at a constant altitude of approximately 30 m above the seafloor, producing swath ranges of 72 m (A17), 158 m (C20), and 88 m (T2-d). The ROV collected video and imagery (D-F) near the three chosen core sites.

Several seafloor observations show localized holes, pits, and small-scale disturbances that may reflect benthic or biogenic activity within otherwise quiescent sediments (Figure

5.5a-f). While the origin and ecological significance of these features remain uncertain, they suggest that biological interactions with contaminated sediments may still occur at localized scales. Such activity could provide potential pathways for contaminant exchange between buried sediments and the surrounding benthic ecosystem, including possible transfer into the marine food web through burrowing or filter-feeding organisms. Together, these observations support the interpretation that present-day hydrodynamic conditions within SPB are generally insufficient to sustain persistent basin-wide erosion, while localized biological reworking and episodic sediment disturbance may still contribute to heterogeneous DDX distributions and sediment exposure at the seafloor.

5.3 Biogenic Processes

Although the observed hydrodynamic conditions in SPB suggest that widespread erosion and persistent sediment resuspension are unlikely under the observed conditions, localized disturbances may still occur through biological influences. ROV and SAS imagery collected from across the basin show widespread small-scale seabed features, including mounds with holes, and irregular features that may indicate active benthic bioturbation. Biological disturbance mechanisms such as burrowing, feeding activity, and sediment reworking may locally change shallow burial horizons or contribute to limited redistribution of contaminated sediments, even in areas where the bottom layer flow is weak. Unlike large-scale physical resuspension events, these processes likely operate over smaller spatial scales and may produce heterogeneous patterns of localized sediment mixing. These observations suggest that while bottom-boundary layer conditions within SPB may be insufficient to sustain widespread erosion, biological activity may be a secondary mechanism that influences contaminant exposure into the local ecology. Additional work is needed to quantify benthic mixing rates, characterize biological disturbance intensity, and evaluate potential trophic transfer pathways associated with persistent DDT and DDX contamination within SPB sediments.

Chapter 6

Conclusions and Future Work

6.1 Conclusions

The observations presented in this study indicate that the deep SPB is characterized by weakly stratified, weakly ventilated bottom waters and relatively low-energy bottom boundary layer dynamics dominated by oscillatory semidiurnal tidal forcing. Hydrographic observations from the SPOT program show minimal variability below the sill depth, with weak seasonal and interannual changes in temperature, density, and dissolved oxygen. The absence of strong hydrographic anomalies during the 2023 and 2024 mooring deployments further suggests that no major flushing events occurred during the observational period, and that the basin remained in a relatively quiescent background state. Together, the SPOT climatology and moored observations support the interpretation that deep SPB waters remain dynamically isolated for extended periods, with limited exchange across the sill and weak vertical ventilation.

Spectral, harmonic, and rotary analyses of the ADCP observations consistently demonstrate that near-bottom flow variability is dominated by semidiurnal tidal motions associated with the M2 and S2 constituents. Variance ellipses and two-dimensional velocity distributions indicate that the flow is largely oscillatory and centered near zero mean velocity, rather than characterized by persistent directional transport. EOF analysis further showed that more than 90% of the observed variance is explained by a single vertically coherent mode, suggesting that the bottom boundary layer behaves primarily as a depth-uniform tidally forced flow with relatively weak higher-order shear structure. Although weaker energy was present at diurnal and near-inertial frequencies, these contributions were secondary relative to the dominant semidiurnal band. Collectively, these observations indicate that near-bottom circulation in SPB is primarily controlled by oscillatory tidal forcing rather than sustained advective currents or energetic renewal flows.

A primary objective of this study was to evaluate whether the observed hydrodynamic conditions within SPB are sufficient to mobilize DDT-contaminated sediments. Initial estimates using the Shields framework provided a useful first-order comparison for unconsolidated sandy sediment, but the applicability of classical Shields theory is limited for the fine-grained silty clay and mud sediments that dominate the SPB seabed. Sediment cores and prior studies indicate that SPB sediments are highly cohesive, water-saturated, and progressively consolidated with depth. As a result, sediment erosion is governed not only by grain size and submerged particle weight but also by electrochemical cohesion, porosity, and consolidation state. These properties substantially increase resistance to erosion compared to noncohesive sandy beds.

To better represent these sediment properties, bed shear stress estimates derived from the ADCP observations were compared against empirical cohesive sediment erosion thresholds parameterized using dry-bulk density. Observed near-bed currents were generally weak, with most velocities remaining below approximately 0.1 m s^{-1}, and resulting drag-law-derived bed shear stresses remained below the modeled critical erosion thresholds for representative cohesive SPB sediments throughout nearly the entire deployment. Although short-lived energetic events intermittently increased bed shear stress, these events were insufficient to indicate widespread or persistent sediment mobilization. While the exact erosion threshold varies among empirical formulations and assumed sediment consolidation states, the overall interpretation remains robust across all tested approaches: hydrodynamic forcing within SPB under typical background conditions is likely insufficient to drive widespread resuspension of cohesive contaminated sediments. The weak near-bottom currents observed at the DS2 mooring are also broadly consistent with recent numerical simulations of circulation within the Southern California Borderland Basins. McWilliams et al. (2024) found that mean currents within SPB are generally weak in the basin interior and strongest along basin margins and sill passages, with modeled mean velocities of approximately 0.011 m s^{-1} along basin slopes [19]. The observed velocities at the mooring site are therefore consistent with a low-energy interior basin environment and support the interpretation that widespread sediment remobilization is unlikely under modern conditions. Furthermore, the model predicts enhanced circulation near basin margins and sill regions, suggesting that localized areas of elevated bed stress may exist outside the region sampled by the mooring.

This interpretation is further supported by the sediment core observations and seafloor imagery. Sediment cores show that maximum DDT and DDX concentrations are commonly buried several centimeters below the sediment-water interface, suggesting long-term burial and limited recent disturbance of the seabed. Acoustic and optical imagery additionally reveal a relatively smooth depositional environment with localized benthic communities and bioturbation features rather than extensive evidence of large-scale erosional scouring or active sediment transport. Localized benthic communities and bioturbation features observed in the imagery suggest biological influences might still rework contaminants in SPB sediments. Despite weak observed near-bottom shear stresses during the mooring deployment, which are likely insufficient to drive basin-wide resuspension, localized burrowing, sediment mixing, and benthic feeding activity may expose contaminated sediments intermittently. These biological influences may provide pathways for contaminants into the benthic ecosystem and into the surrounding marine food web. These observations suggest that contaminant retention within the basin is promoted by the combined effects of weak deep circulation, restricted basin geometry, cohesive sediment properties, and limited bottom shear stress.

Although widespread hydrodynamically driven resuspension appears unlikely under the observed conditions, the results do not preclude localized or episodic sediment mobilization. Energetic flushing events, dense overflow currents, internal wave activity, slope failures, benthic organism activity, or anthropogenic disturbance may still intermittently resuspend contaminated material on local scales. Additionally, the observational record is limited to a relatively short deployment period that did not capture a major deep-water renewal event. Future studies integrating longer-duration moorings, turbulence measurements, sediment traps, and direct benthic stress observations would help constrain the role of episodic forcing and biological processes in sediment redistribution and contaminant exposure pathways.

Overall, this study suggests that the deep San Pedro Basin functions as a relatively quiescent depositional environment where weak tidal oscillations dominate near-bottom flow variability and promote long-term retention of contaminated sediments within the basin.

6.2 Future Work

While this study provides insight into the hydrodynamic conditions and the potential for sediment mobility within SPB, several important questions remain regarding the processes controlling contaminant remobilization and transport. The present analysis is based on observations from a single mooring location and therefore may not capture the full spatial variability in the basin's bottom boundary layer dynamics. Additional long-term observations and numerical modeling efforts would improve understanding of episodic renewal events and interannual variability that may not have been captured during the 2024 deployment period. Future studies should also investigate how the geometry of SPB influences circulation patterns and sediment transport pathways. The constricted region between Santa Catalina Island and Redondo Knoll may influence currents and increase bed stresses relative to the 2024 mooring site due to bathymetric steering.

Although the hydrodynamic analysis suggests that widespread physical erosion of the basin sediments is unlikely under the observed conditions, biological disturbance may represent an important mechanism for localized sediment reworking and contaminant exposure. ROV and SAS imagery revealed numerous mounds and depression-like seabed features that show evidence of burrowing activity. These are found predominantly around the margins of the basin near the Palos Verdes shelf and slope [23]. Future work should quantify the morphology, spatial distribution, and abundance of these features using image-based analyses. This analysis should

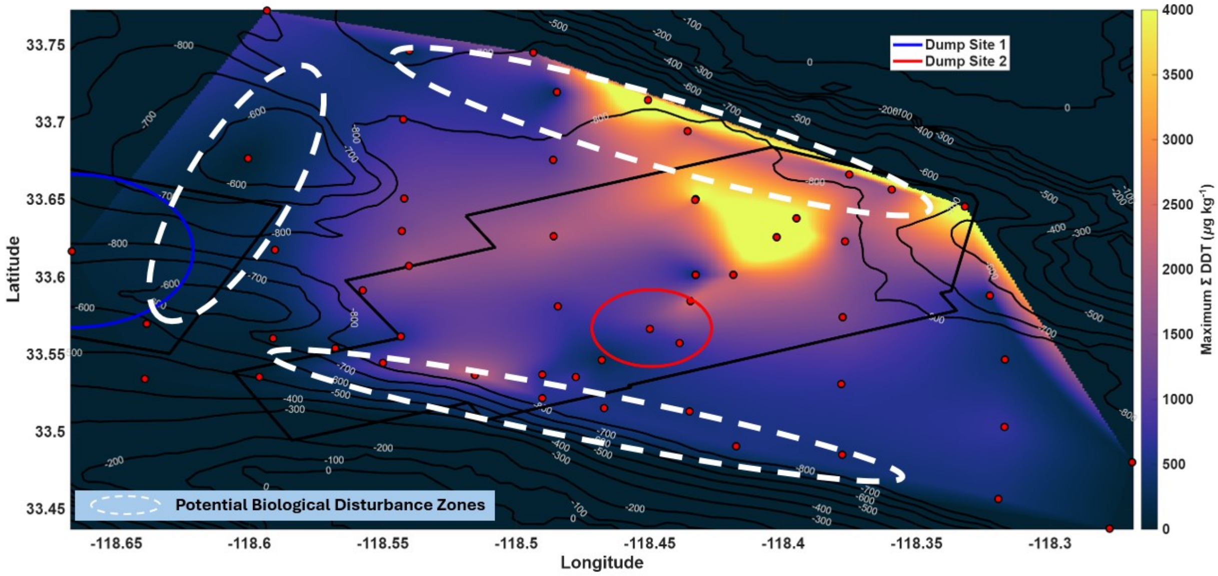

Figure 6.1. The colored surface shows the spatial distribution of maximum ΣDDT concentrations from sediment cores. White dashed outlines identify basin-margin regions prioritized for future investigation of biological disturbance processes based on observations of mound- and depression-like seabed features in available imagery.

be a collaborative effort with a marine biology-focused group to better use the physical framing of seabed morphology alongside the identification and classification of benthic communities that serve as possible trophic transfer pathways. The effort may help determine whether biological activity influences the preservation, redistribution, or exposure of contaminants in SPB's sediments.

Additional sediment coring efforts would further improve understanding of contaminant burial histories and sediment stability throughout SPB. Greater coverage of basin margins, regions of observed biological disturbance, and areas exhibiting shallow contaminant burial depths would help determine whether localized sediment mixing contributes to the observed spatial variability in contaminant distributions. Improved characterization of how bioturbation processes contributes to the preservation, redistribution, or exposure of contaminants within SPB sediments.

The results of this study suggest that widespread physical remobilization of contaminated sediments is unlikely under the observed conditions. The presence of biological disturbance structures throughout portions of the basin indicates that non-hydrodynamic processes may contribute to localized sediment mixing and contaminant exposure. Future models should incorporate hydrodynamic forcing, sediment transport, biodiffusion, and bioturbation within a unified framework to evaluate the long-term stability of contaminated sediments. Such an approach would help determine whether the redistribution of contaminants is primarily controlled by episodic physical transport events, bioturbation, or interactions between the two processes. Together, these efforts would provide a more complete understanding of contaminant preservation, exposure pathways, and long-term environmental risk within SPB.

Bibliography

[1] Critical Thresholds for Transport and Erosion.

[2] John Beard. DDT and human health. *Science of The Total Environment*, 355(1):78–89, February 2006.

[3] Steven J. Bograd, Mercedes Pozo Buil, Emanuele Di Lorenzo, Carmen G. Castro, Isaac D. Schroeder, Ralf Goericke, Clarissa R. Anderson, Claudia Benitez-Nelson, and Frank A. Whitney. Changes in source waters to the Southern California Bight. *Deep Sea Research Part II: Topical Studies in Oceanography*, 112:42–52, February 2015.

[4] Dake Chen, Jinhai Zheng, Chi Zhang, Dawei Guan, Yuan Li, and Huiming Huang. Threshold of surface erosion of cohesive sediments. *Frontiers in Marine Science*, 9, September 2022.

[5] Lisa E. Collins, William Berelson, Douglas E. Hammond, Angela Knapp, Richard Schwartz, and Doug Capone. Particle fluxes in San Pedro Basin, California: A four-year record of sedimentation and physical forcing. *Deep Sea Research Part I: Oceanographic Research Papers*, 58(8):898–914, August 2011.

[6] Peter Dartnell, Emily C. Roland, Nicole A. Raineault, Christopher M. Castillo, James E. Conrad, Renato Kane, Daniel S. Brothers, Jared W. Kluesner, and Maureen A. L. Walton. Colored shaded-relief bathymetry, acoustic backscatter, and selected perspective views of the northern part of the California Continental Borderland, southern California. Technical Report 3473, U.S. Geological Survey, 2021. Publication Title: Scientific Investigations Map.

[7] E.A. Delo and T.N. Burt. The Hydraulic Engineering Characteristics of Estuarine Muds: A Working Manual and Literature Review. Technical Report SR 77, Hydraulics Research Limited, Wallingford, Oxfordshire, UK, December 1986.

[8] Bénédicte Ferré, Christopher R. Sherwood, and Patricia L. Wiberg. Sediment transport on the Palos Verdes shelf, California. *Continental Shelf Research*, 30(7):761–780, April 2010.

[9] D. Michael Fry. Reproductive Effects in Birds Exposed to Pesticides and Industrial

Chemicals. *Environmental Health Perspectives*, 103:165–171, 1995.

[10] D.S. Gorsline. The geological setting of Santa Monica and San Pedro Basins, California Continental Borderland. *Progress in Oceanography*, 30(1-4):1–36, January 1992.

[11] Johanna Gutleben, Sheila Podell, Kira Mizell, Douglas Sweeney, Carlos Neira, Lisa A Levin, and Paul R Jensen. Extremophile hotspots linked to containerized industrial waste dumping in a deep-sea basin. *PNAS Nexus*, 4(9):pgaf260, September 2025.

[12] Barbara M. Hickey. Circulation over the Santa Monica-San Pedro Basin and Shelf. *Progress in Oceanography*, 30(1-4):37–115, 1992.

[13] Barbara M Hickey. Basin-to-basin water exchange in the Southern California Bight. In D.R. Browne, K.L. Mitchell, and H.W. Chaney, editors, *Proceedings of the Fifth California Islands Symposium*, pages 89–92. Minerals Management Service, Camarillo, CA, 2000.

[14] Sung Yong Kim and Bruce D. Cornuelle. Coastal ocean climatology of temperature and salinity off the Southern California Bight: Seasonal variability, climate index correlation, and linear trend. *Progress in Oceanography*, 138:136–157, November 2015.

[15] Veronika Kivenson, Karin L. Lemkau, Oscar Pizarro, Dana R. Yoerger, Carl Kaiser, Robert K. Nelson, Catherine Carmichael, Blair G. Paul, Christopher M. Reddy, and David L. Valentine. Ocean Dumping of Containerized DDT Waste Was a Sloppy Process. *Environmental Science & Technology*, 53(6):2971–2980, March 2019.

[16] Andreas Lorke, Lars Umlauf, Tobias Jonas, and Alfred Wüest. Dynamics of Turbulence in Low-Speed Oscillating Bottom-Boundary Layers of Stratified Basins. *Environmental Fluid Mechanics*, 2(4):291–313, December 2002.

[17] Susan A. Mackintosh, Nathan G. Dodder, Nellie J. Shaul, Lihini I. Aluwihare, Keith A. Maruya, Susan J. Chivers, Kerri Danil, David W. Weller, and Eunha Hoh. Newly Identified DDT-Related Compounds Accumulating in Southern California Bottlenose Dolphins. *Environmental Science & Technology*, 50(22):12129–12137, November 2016.

[18] Lillian McGill, Toni Sleugh, Colleen Petrik, Kenneth Schiff, Karen McLaughlin, Lihini Aluwihare, and Brice Semmens. The persistent DDT footprint of ocean disposal, and ecological controls on bioaccumulation in fishes. *Proceedings of the National Academy of Sciences*, 121(45):e2401500121, November 2024.

[19] James C. McWilliams, Pierre Damien, and Faycal Kessouri. Circulation and dispersal in California's Borderland Basins. *Progress in Oceanography*, 229:103349, December 2024.

[20] Sophia T. Merrifield, Sean Celona, Ryan A. McCarthy, Andrew Pietruszka, Heidi Batchelor, Robert Hess, Andrew Nager, Raymond Young, Kurt Sadorf, Lisa A. Levin, David L.

Valentine, James E. Conrad, and Eric J. Terrill. Wide-Area Debris Field and Seabed Characterization of a Deep Ocean Dump Site Surveyed by Autonomous Underwater Vehicles. *Environmental Science & Technology*, 57(46):18162–18171, November 2023.

[21] Carlos Neira, Guillermo F. Mendoza, Angelica Bradley, Richard Gossett, Greg W. Rouse, and Lisa A. Levin. Waste barrel contamination and macrobenthic communities in the San Pedro Basin DDT dumpsite. *Marine Pollution Bulletin*, 203:116463, June 2024.

[22] Jacob T. Schmidt, Mong Sin Christine Wu, Hailie E. Kittner, J. Samuel Arey, Douglas E. Hammond, Earth 182A Group, and David L. Valentine. Disentangling the History of Deep Ocean Disposal for DDT and Other Industrial Waste Off Southern California. *Environmental Science & Technology*, 58(9):4346–4356, March 2024.

[23] Janet K. Stull, Donald J. P. Swift, and Alan W. Niedoroda. Contaminant dispersal on the Palos Verdes continental margin: I. Sediments and biota near a major California wastewater discharge. *Science of The Total Environment*, 179:73–90, January 1996.

[24] Margaret Sullivan, Eric Terrill, Ryan A. McCarthy, Sean Celona, and Sophia Merrifeild. Characterization of a Deep Ocean Dump Site: Seabed Survey and Oceanographic Context. In *OCEANS 2023 - MTS/IEEE U.S. Gulf Coast*, pages 1–5, Biloxi, MS, USA, September 2023. IEEE.

[25] Robert C. Thunell, Cynthia H. Pilskaln, Eric Tappa, and Leslie Reynolds Sautter. Temporal variability in sediment fluxes in the San Pedro Basin, southern California bight. *Continental Shelf Research*, 14(4):333–352, April 1994.

[26] John H. Trowbridge and Steven J. Lentz. The Bottom Boundary Layer. *Annual Review of Marine Science*, 10(1):397–420, January 2018.

[27] University of Southern California. Home.

[28] U.S. Army Corps of Engineers Hydrologic Engineering Center. Crticial Thresholds for Transport and Erosion. Technical report.

[29] U.S. Army Corps of Engineers Hydrologic Engineering Center. Final Report for the Summer 2004 Sediment Displacement Study on the Palos Verdes Shelf. Technical report.

[30] Mong Sin Christine Wu, Jacob T. Schmidt, Hailie E. Kittner, Earth 182B Group, and David L. Valentine. Geospatial and Temporal Inventory for Industrial DDT Waste Disposal to a Deep Coastal Ocean Environment. *Environmental Science & Technology*, 59(38):20578–20587, September 2025.

[31] Weiming Wu, Chamil Perera, Jarrell Smith, and Alejandro Sanchez. Critical shear stress for erosion of sand and mud mixtures. *Journal of Hydraulic Research*, 56(1):96–110, January

2018. _eprint: https://doi.org/10.1080/00221686.2017.1300195.